Topological Semimetals

by

Michael Hook

A thesis
presented to the University of Waterloo
in fulfillment of the
thesis requirement for the degree of
Master of Science
in
Physics

Waterloo, Ontario, Canada, 2012

I hereby declare that I am the sole author of this thesis. This is a true copy of the thesis, including any required final revisions, as accepted by my examiners.

I understand that my thesis may be made electronically available to the public.

Abstract

This thesis describes two topological phases of matter, the Weyl semimetal and the line node semimetal, that are related to but distinct from topological insulator phases. These new topological phases are semimetallic, having electronic energy bands that touch at discrete points or along a continuous curve in momentum space. These states are achieved by breaking time-reversal symmetry near a transition between an ordinary insulator and a topological insulator, using a model based on alternating layers of topological and ordinary insulators, which can be tuned close to the transition by choosing the thicknesses of the layers. The semimetallic phases are topologically protected, with corresponding topological surface states, but the protection is due to separation of the band-touching points in momentum space and discrete symmetries, rather than being protected by an energy gap as in topological insulators. The chiral surface states of the Weyl semimetal give it a non-zero Hall conductivity, while the surface states of the line node semimetal have a flat energy dispersion in the region bounded by the line node. Some transport properties are derived, with a particular emphasis on the behaviour of the conductivity as a function of the impurity concentrations and the temperature.

Acknowledgements

Table of Contents

List of Figures

Chapter 1

Introduction: Topological Insulators

In recent years, there has been considerable interest in a new class of materials known as time-reversal invariant topological insulators (TIs). These materials are characterized by the combination of a gap in the bulk electron energy spectrum and gapless surface states. The surface states are guaranteed by a quantity called a topological invariant,[13] which is unaffected by continuous changes to the system, provided that such changes do not close the bulk energy gap. Thus, the stability of TIs depends crucially on the gap.[21]

Recent work has shown, however, that there are other systems with nontrivial topological invariants and corresponding surface states, but no bulk gap. Instead, two bands touch at special points in the Brillouin zone. A different mechanism is then required to stabilize the surface states. In this thesis, I describe a simple, experimentally feasible realization of this type of system; two distinct semimetal phases are produced by adding different TR symmetry-breaking perturbations to the system of stacked topological and ordinary insulator layers described in Section 2.[2, 3, 24]

This thesis is organized as follows. Chapter 1 introduces the concepts of topological invariants and surface states in more detail and discusses transitions between ordinary insulating and topological insulator phases, using the quantum spin Hall state in graphene as an example. Chapter 2 introduces a model structure of alternating layers of ordinary and topological insulator layers and examines the limiting case of a single TI layer in more detail. Chapters 3 and 5 discuss recently proposed topological phases that arise in the layered structure when time-reversal symmetry is broken. Finally, Chapter 5 discusses transport properties of these topological phases, with the hope that these properties may be experimentally observable and aid in identification of these phases in real systems.
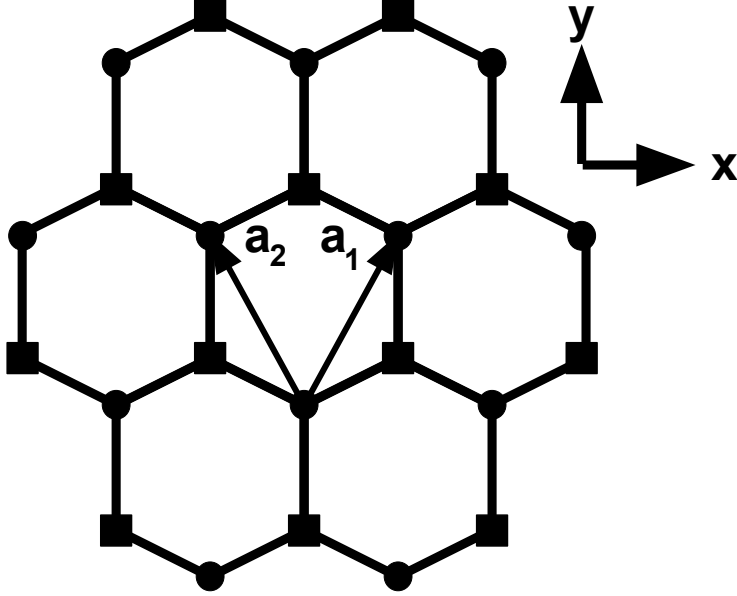
Figure 1.1: Honeycomb structure of graphene, showing lattice vectors $\mathbf{a}_1$ and $\mathbf{a}_2$. Dots and squares represent carbon atoms in sublattices 1 and 2, respectively.

1.1 Graphene

1.1.1 Band Structure

The properties of two-dimensional TIs can be explained by Kane and Mele's model of graphene with spin-orbit coupling.[12] Graphene is a two-dimensional crystal consisting of carbon atoms arranged in a honeycomb structure with two hexagonal sublattices offset from each other as shown in Figure 1.1.[7] Graphene itself has attracted considerable interest for its unusual electronic properties [23, 18, 8, 20, 4, 5], which are similar in many ways to those of the materials described later in this thesis.

For low energies, an effective Hamiltonian for graphene can be computed by using a tight-binding description, beginning with the Hamiltonian [22]

$$\mathcal{H} = -t \sum_{<i\alpha,j\beta>} \left[c_{i\alpha}^\dagger c_{j\beta} + c_{j\beta}^\dagger c_{i\alpha} \right], \tag{1.1}$$

where the sum runs over nearest neighbour atoms on lattice sites i, j and sublattices $\alpha, \beta \in \{1, 2\}$, $c_{i\alpha}$ is the annihilation operator for an electron at lattice site i on sublattice α, and $c_{i\alpha}^\dagger$ is the corresponding creation operator. Spin has been temporarily neglected. Applying
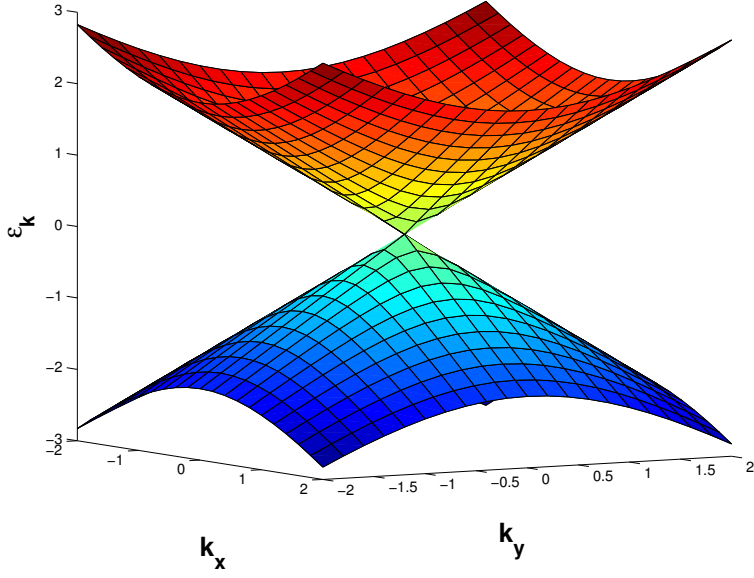
Figure 1.2: Plot of the distinctive "Dirac cone" dispersion of graphene, $\epsilon_{\mathbf{k}} = \hbar v_F |\mathbf{k}|$. The energy of an electron is directly proportional to its momentum and there is no energy gap; electronic states are available at all energies (in the small momentum approximation that leads to Equation (1.4).

a Fourier transform,

$$c_{j\alpha}^{\dagger} = \frac{1}{\sqrt{N}} \sum_{\mathbf{k},\alpha} c_{\mathbf{k}\alpha}^{\dagger} e^{-i\mathbf{k}\cdot\mathbf{R}_j}, \tag{1.2}$$

where N is the number of lattice sites, leads to the momentum-space Hamiltonian

$$\mathcal{H} = -t \sum_{\mathbf{k}} \left[c_{\mathbf{k}1}^{\dagger} c_{\mathbf{k}2} \left(1 + e^{-i\mathbf{k}\cdot\mathbf{a}_1} + e^{-i\mathbf{k}\cdot\mathbf{a}_2} \right) + c_{\mathbf{k}2}^{\dagger} c_{\mathbf{k}1} \left(1 + e^{i\mathbf{k}\cdot\mathbf{a}_1} + e^{i\mathbf{k}\cdot\mathbf{a}_2} \right) \right]. \tag{1.3}$$

This Hamiltonian has two independent band-touching points at $k_x = \pm\frac{4\pi}{3a}$, where $a = |\mathbf{a}_1| = |\mathbf{a}_2|$. Expanding the Hamiltonian at low energies near these points gives the effective Hamiltonian

$$\mathcal{H}_0(\mathbf{k}) = \hbar v_F (k_x \sigma^x \tau^z + k_y \sigma^y), \tag{1.4}$$

where $v_F = \frac{\sqrt{3}ta}{2\hbar}$ and $\boldsymbol{\sigma}$ and $\boldsymbol{\tau}$ are Pauli operators acting on pseudospin degrees of freedom: $\boldsymbol{\sigma}$ describes which sublattice the electron is on and $\boldsymbol{\tau}$ describes which band-touching point it is near in momentum space. The Hamiltonian (1.4) describes a massless Dirac fermion (the general theory of which will be discussed in Section 1.2), with the dispersion near each band-touching point having the well-known Dirac cone form $\epsilon_{\mathbf{k}} = \hbar v_F |\mathbf{k}|$, shown in Figure 1.2.

3

1.1.2 Spin-Orbit Coupling

In [12], Kane and Mele considered the addition of another term to (1.4), arising from spin-orbit coupling:

$$\mathcal{H}_{SO}(\mathbf{k}) = \Delta_{SO}\sigma^z\tau^z s^z, \tag{1.5}$$

with s^z a Pauli operator acting on spin. This term respects both the inversion symmetry (which inverts σ^z and τ^z) and the time-reversal symmetry (which inverts τ^z and s^z) of graphene, but gives a non-zero mass to the Dirac fermions of (1.4) and leads to the dispersion $\epsilon_{\mathbf{k}} = \pm\sqrt{(\hbar v_F k)^2 + \Delta_{SO}^2}$, with an energy gap $2\Delta_{SO}$. Such a Dirac mass, with a corresponding energy gap, also arises from, for instance, a σ^z term, corresponding to a potential with opposite signs on the two sublattices. The resulting system would be topologically trivial, as in the limit of an infinitely strong potential, it simply decouples the two sublattices, creating an atomic insulator, wherein conduction does not occur because electrons are unable to travel from one atom to its nearest neighbour because of the large energy barrier. As will be shown, however, the spin-orbit term leads to a non-trivial topology, meaning the system cannot be continuously transformed to a trivially insulating phase without closing the energy gap at some intermediate stage.

Including both the spin-orbit term of (1.5) and a mass term $m\sigma^z$ as mentioned above, the Hamiltonian is

$$\mathcal{H}(\mathbf{k}) = \hbar v_F(k_x\sigma^x\tau^z + k_y\sigma^y) + \Delta_{SO}\sigma^z\tau^z s^z + m\sigma^z. \tag{1.6}$$

The three sets of Pauli operators in (1.6) commute with one another, so it is clear that both τ^z and s^z commute with $\mathcal{H}(\mathbf{k})$, meaning that they can be diagonalized simultaneously with $\mathcal{H}(\mathbf{k})$. Thus, beginning with the case $s^z = 1$, one can write

$$\mathcal{H}_{\pm}(\mathbf{k}) = \hbar v_F(\pm k_x\sigma^x + k_y\sigma^y) + (m \pm \Delta_{SO})\sigma^z, \tag{1.7}$$

with the plus and minus signs corresponding to the eigenvalues of τ^z, i.e., the two Dirac points. The key feature of this equation is the sign change of the Dirac mass $m \pm \Delta_{SO}$ in the $\mathcal{H}_-$ block; the $m > \Delta_{SO}$ and $m < \Delta_{SO}$ cases can be distinguished by examining the Landau level spectra of the two blocks.

1.1.3 Landau Level Spectra

The Landau level spectra are found by introducing a magnetic field perpendicular to the plane of the sample: $\mathbf{B} = B\hat{z}$, which is equivalently described by the vector potential

$\mathbf{A} = xB\hat{y}$ in what is known as the Landau gauge. In a position space representation, $\hbar\mathbf{k}$ becomes $-i\hbar\nabla + \frac{e}{c}\mathbf{A}$, giving

$$\mathcal{H}_\pm = \mp i\hbar v_F \frac{\partial}{\partial x}\sigma^x + \hbar v_F \left(-i\frac{\partial}{\partial y} + \frac{x}{\ell^2} \right)\sigma^y + (m \pm \Delta_{SO})\sigma^z, \tag{1.8}$$

where $\ell = \sqrt{\frac{\hbar c}{eB}}$ is the magnetic length.

Examining $\mathcal{H}_\pm^2$ simplifies the calculation of the Landau level spectrum. Noting that the Pauli operators anticommute with one another and square to the identity operator, and also that $\left[\frac{\partial}{\partial x}, x \right] = 1$, one can calculate

$$\mathcal{H}_\pm^2 = -\hbar^2 v_F^2 \frac{\partial^2}{\partial x^2} + \hbar^2 v_F^2 \left(-i\frac{\partial}{\partial y} + \frac{x}{\ell^2} \right)^2 + (m \pm \Delta_{SO})^2 \pm \hbar^2 \omega_B^2 \sigma^z, \tag{1.9}$$

where $\omega_B = v_F/\ell$. All pairs of terms in (1.9) commute, except the first two, and therefore they can be diagonalized independently of one another. The first two terms have eigenstates of the form $\Psi(x,y) = e^{iky}\phi(x)$, giving

$$-\hbar^2 v_F^2 \frac{\mathrm{d}^2\phi}{\mathrm{d}x^2} + \hbar^2 v_F^2 \left(k + \frac{x}{\ell^2} \right)^2 = E\phi(x). \tag{1.10}$$

This is simply the time-independent Schrödinger equation for a one-dimensional harmonic oscillator centred away from the origin, with the mass replaced by $1/2v_F^2$ and the frequency by $2\hbar\omega_B^2$. Since the energy levels of a harmonic oscillator are given by $E_n = \hbar\omega(n + 1/2)$, Equation (1.9) can be written as

$$\mathcal{H}_\pm^2 = 2\hbar^2\omega_B^2(n + \frac{1}{2}) \pm \hbar^2\omega_B^2\sigma^z + (m \pm \Delta_{SO})^2, \tag{1.11}$$

where n can be any non-negative integer.

The resulting Landau level energies satisfy

$$|\epsilon_{N\pm}| = \sqrt{2\hbar^2\omega_B^2 N + (m \pm \Delta_{SO})^2}, \tag{1.12}$$

with $N = n$ or $N = n+1$ depending on the action of σ^z on the state. For $N \geq 1$, there are two solutions for $|\epsilon_{N\pm}|$ with the same magnitude and opposite sign. For N = 0, however, there is only one solution for each block of the Hamiltonian, with the signs determined by the eigenvalue of σ^z: for ϵ_{0+}, $\langle \sigma^z \rangle = -1$ and (1.8) requires that the coefficient of $m + \Delta_{SO}$ be negative. Likewise, the coefficient of $m - \Delta_{SO}$ is positive for ϵ_{0-}. Thus, the Landau
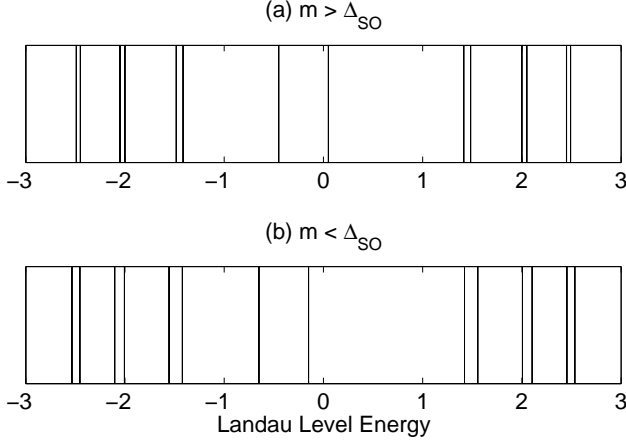
Figure 1.3: Landau level spectra of graphene for $s^z = 1$ with staggered potential m and spin-orbit coupling Δ_{SO}. (a) $m > \Delta_{SO}$. (b) $m < \Delta_{SO}$. Notice that one Landau level crosses the zero energy point, moving from positive energy in (a) to negative energy in (b). If the Fermi energy is held fixed at $\epsilon_F = 0$, this level becomes filled for $\Delta_{SO} > m$, contributing a Hall conductance e^2/h.

levels for $N \geq 1$ are symmetric about zero energy, but those for $N = 0$ are not: the energies are

$$\epsilon_{0+} = -(m + \Delta_{SO}), \text{ and} \tag{1.13}$$

$$\epsilon_{0-} = m - \Delta_{SO}. \tag{1.14}$$

The sign change of ϵ_{0-} at $m = \Delta_{SO}$ reveals the topological nature of the $\Delta_{SO} > m$ state: if the Fermi energy remains fixed at $\epsilon_F = 0$, there is one extra filled Landau level when $\Delta_{SO} > m$, resulting in a Hall conductance of e^2/h, whereas the Hall conductance for $m > \Delta_{SO}$ is zero.

The above calculation was for electrons with spins aligned parallel to the field; for anti-parallel spins, a similar calculation gives

$$\epsilon_{0+} = -(m - \Delta_{SO}) \text{ and} \tag{1.15}$$

$$\epsilon_{0-} = m + \Delta_{SO}. \tag{1.16}$$

So in this case, there is an extra *unfilled* Landau level when $\Delta_{SO} > m$, contributing a Hall conductance $-e^2/h$ that cancels the above contribution. But although the net Hall conductance is zero, these two sets of Landau states for $\Delta_{SO} > m$ remain distinct, describing electrons with opposite spins that travel in opposite directions along the edge of the material. This results in a spin current $\mathbf{J}_s = (\hbar/2e)(\mathbf{J}_\uparrow - \mathbf{J}_\downarrow)$, where $\mathbf{J}_\uparrow$ and $\mathbf{J}_\downarrow$ are the charge current contributions from spin-up and spin-down electrons, respectively. The corresponding spin Hall conductivity is then quantized as $\sigma_{xy}^s = e/2\pi$. [12]

6
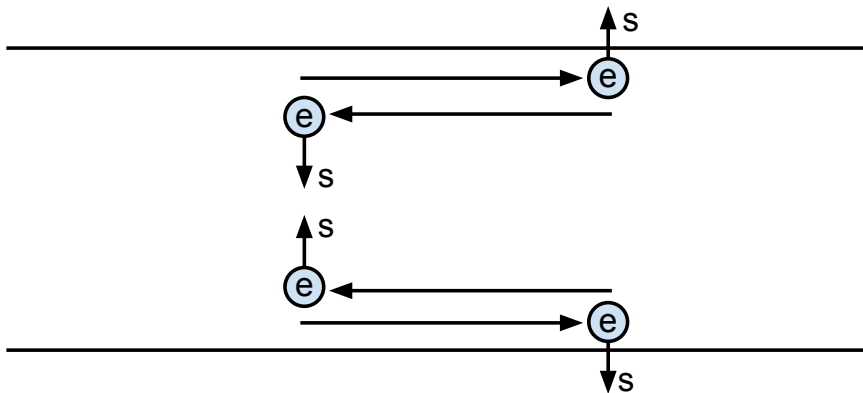
Figure 1.4: Illustration of the edge states of a two-dimensional TI or Quantum spin Hall insulator. Electrons of opposite spin move in opposite directions around the edge of the material.

The energies of the $N = 0$ Landau levels calculated above are completely independent of the magnitude of B, meaning that the spin Hall conductivity remains even in the limit $B \to 0$. In this limit, the time-reversal symmetry of the system, broken by the applied magnetic field, is restored.

The existence of topological edge states in the limit $B \to 0$ can be demonstrated by explicitly solving the time-independent Schrödinger equation corresponding to Equation (1.7), a method that is demonstrated in Section 2.1.3.

1.2 Dirac Fermions

A three-dimensional Dirac fermion is an excitation described by the Dirac Hamiltonian

$$\mathcal{H} = \sum_{\mathbf{k}} \left[\sum_{\mu=1}^{3} k_\mu \gamma_\mu + m \gamma_4 \right] c_{\mathbf{k}}^\dagger c_{\mathbf{k}}, \tag{1.17}$$

where k_μ is the μth component of the (dimensionless) momentum, m is the mass of the Dirac fermion, and γ_μ are Hermitian matrices that describe a discrete degree of freedom such as spin, and satisfy [6]

$$\gamma_\mu^2 = 1 \text{ and } \gamma_\mu \gamma_\nu + \gamma_\nu \gamma_\mu = 0 \text{ for } \mu \neq \nu. \tag{1.18}$$

7

For non-zero m, the Dirac matrices must be 4×4 in size. For example, Section 2.2 will describe a system with a Dirac Hamiltonian corresponding to the 4×4 matrices

$$\gamma_1 = \begin{pmatrix} -\sigma^y & 0 \\ 0 & \sigma^y \end{pmatrix}, \gamma_2 = \begin{pmatrix} \sigma^x & 0 \\ 0 & -\sigma^x \end{pmatrix}, \gamma_3 = \begin{pmatrix} 0 & -iI \\ iI & 0 \end{pmatrix}, \text{and } \gamma_4 = \begin{pmatrix} 0 & I \\ I & 0 \end{pmatrix}. \tag{1.19}$$

The full Hamiltonian of Equation (1.17) can then be written as

$$\mathcal{H}(\mathbf{k}) = \begin{pmatrix} 0 & i(k_x - ik_y) & -ik_z + m & 0 \\ -i(k_x + ik_y) & 0 & 0 & -ik_z + m \\ ik_z + m & 0 & 0 & -i(k_x - ik_y) \\ 0 & ik_z + m & i(k_x + ik_y) & 0 \end{pmatrix}. \tag{1.20}$$

Alternatively, one can choose the representation

$$\gamma_1 = \begin{pmatrix} \sigma^x & 0 \\ 0 & \sigma^x \end{pmatrix}, \gamma_2 = \begin{pmatrix} \sigma^y & 0 \\ 0 & \sigma^y \end{pmatrix}, \gamma_3 = \begin{pmatrix} \sigma^y & 0 \\ 0 & \sigma^y \end{pmatrix}, \gamma_4 = \begin{pmatrix} 0 & I \\ I & 0 \end{pmatrix}. \tag{1.21}$$

The Dirac Hamiltonian can then be written in the form

$$\mathcal{H}(\mathbf{k}) = \begin{pmatrix} \boldsymbol{\sigma} \cdot \mathbf{k} & m \\ m & -\boldsymbol{\sigma} \cdot \mathbf{k} \end{pmatrix}. \tag{1.22}$$

The 2×2 blocks $\pm \boldsymbol{\sigma} \cdot \mathbf{k}$ describe two-component Dirac fermions, since the three 2×2 Pauli matrices also satisfy the property (1.18) required of the Dirac matrices. These two-component Dirac fermions are known as Weyl fermions,[19] and individual Weyl fermions in three dimensions must be massless, since there is no fourth 2×2 matrix that can satisfy (1.18) with the Pauli matrices, and hence there cannot be a mass term in Equation (1.17).

With a non-zero mass in Equation (1.22), the two Weyl fermions are coupled, creating a gap in the energy spectrum, $\epsilon(\mathbf{k}) = \pm\sqrt{k^2 + m^2}$. But with zero mass, the gap closes, yielding the same Dirac cone dispersion found in graphene and shown in Figure 1.2: $\epsilon(\mathbf{k}) = \pm|\mathbf{k}|$. By perturbing the system, for instance by applying a magnetic field to break time-reversal symmetry, the Weyl fermions can be separated in momentum space, preventing them from coupling.

As illustrated in Section 1.1, a sign change of the Dirac mass implies a change in the topology of the system and a quantum Hall transition, resulting from a sign change in the lowest Landau level of the system.[21, 16]

1.3 History and Properties of Topological Insulators

The example of graphene with spin-orbit coupling described in Section 1.1 is an example of a two-dimensional topological insulator, also known as a quantum spin Hall insulator. These are insulators that are topologically distinct from ordinary band insulators, meaning that it is impossible to continuously modify their Hamiltonians into that of an ordinary insulator (for example, a vacuum) without closing the energy gap at some intermediate step. The first known example of such a state was the two-dimensional quantum Hall state discovered in 1980 by von Klitzing et al.[21] This state is achieved by applying a strong magnetic field perpendicular to a thin layer of high-purity conducting material. The magnetic field modifies the electronic orbits, resulting in a set of highly degenerate Landau level states at discrete energies. These Landau states correspond to chiral orbits, traveling in only one direction (determined by the magnetic field) around the edge of the sample. If an integer number of Landau levels are filled, this integer is a topological invariant for the system. This invariant is closely tied to an experimentally measurable quantity: the Hall conductance of the system is $\nu e^2/h$, where ν is the number of filled Landau levels.[21] This quantized Hall conductance allows for very precise measurements of the fine structure constant $\alpha = e^2/\hbar c$, since c is known precisely by the definition of the metre.

Development of these ideas continued with Haldane's theoretical model of a quantum Hall system without an external magnetic field or Landau levels, but with time-reversal symmetry still broken.[9] The quantum spin Hall state of Section 1.1 was predicted to occur in graphene by Kane and Mele in 2005,[12] but the magnitude of the spin-orbit coupling Δ_{SO} has proven to be extremely small, preventing experimental observation of the QSH state in graphene.[21] However, the QSH state was also predicted and later observed in HgTe/CdTe quantum wells.[1, 14]

There are also three-dimensional analogues of the quantum spin Hall state, possessing TR symmetry and helical edge states, meaning that the motion of an electron is coupled to its spin, as in Figure 1.4. They can be classified into strong and weak topological insulators; the weak systems, unlike the strong systems, are equivalent to a stack of two-dimensional systems and not robust in the presence of disorder.[10] The strong topological insulator phase was first observed in antimony-doped bismuth, with the transition from an ordinary insulator to a topological insulator occurring at an antimony concentration of about 4%. This material has a complicated surface electronic structure and a small bulk energy gap.[21] Other strong TIs with simpler surface band structures and larger bulk gaps include Bi_2Se_3, Bi_2Te_3, and Sb_2Te_3. These have bulk gaps between 0.2 and 0.3 eV, meaning that the TI phase is observable even at room temperature ($k_B T \sim 0.025$ eV, about
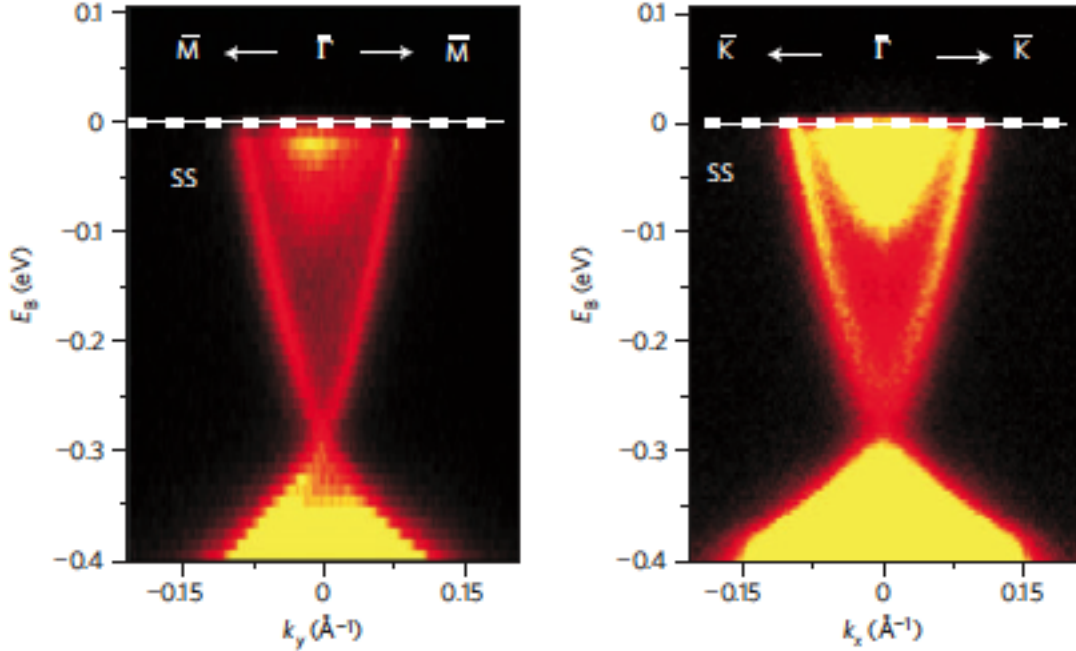
Figure 1.5: Angle-resolved photoemission spectroscopy measurement of the electronic energies of Bi_2Se_3 as a function of electron momentum. The nearly straight lines intersecting at $k_x = 0$ and $k_y = 0$ represent the Dirac surface states, while the solid regions, separated by a vertical gap, represent the bulk states.

10 times smaller).[21] Xia et al. [25] demonstrated the existence of the surface Dirac cone in Bi_2Se_3 using angle-resolved photoemission spectroscopy (ARPES), in which electrons are ejected from a sample by photons of known energy. The momenta of the electrons are then measured, allowing the electronic band structure of both the bulk and the surface to be determined. The results, clearly showing the surface Dirac cone as well as the bulk energy gap, are shown in Figure 1.5.

Near the Dirac point (to second order in momentum), these materials can be described by the Hamiltonian [21]

$$
\mathcal{H}(\mathbf{k}) = \epsilon_0(\mathbf{k}) + \begin{pmatrix} \mathcal{M}(\mathbf{k}) & A_1 k_z & 0 & A_2 k_- \\ A_1 k_z & -\mathcal{M}(\mathbf{k}) & A_2 k_- & 0 \\ 0 & A_2 k_+ & \mathcal{M}(\mathbf{k}) & -A_1 k_z \\ A_2 k_+ & 0 & -A_1 k_z & -\mathcal{M}(\mathbf{k}) \end{pmatrix},
\tag{1.23}
$$

where $k_\pm = k_x \pm i k_y$, $\epsilon_0(\mathbf{k}) = C + D_1 k_z^2 + D_2 k_\perp^2$, and $\mathcal{M}(\mathbf{k}) = M - B_1 k_z^2 - B_2 k_\perp^2$. This

10

Hamiltonian represents a Dirac fermion as in Section 1.2, but with momentum-dependent mass and a additional momentum-dependent energy shift. In more detail, the C term shifts both bands uniformly in energy (representing a change in the chemical potential), the D_1 and D_2 terms shift both energy bands non-uniformly in the same direction, creating particle hole asymmetry, which clearly occurs in the experimental data of Figure 1.5. A_1 and A_2 represent the velocities of electrons along the z axis and in the x-y plane, respectively. M determines the size of the bulk energy gap at the Dirac point, while B_1 and B_2 give the electrons a quadratic dispersion (rather than a linear one, as would otherwise be the case) away from the Dirac point, representing an ordinary non-relativistic mass.

1.4   Time-Reversal Symmetry

This work will make frequent reference to TR symmetry, and most of the results will depend on broken TR symmetry, so it is important to introduce it formally and discuss its role in TI systems. The time-reversal operator $\mathcal{T}$ acts on a Hamiltonian $\mathcal{H}(\mathbf{k})$ as [10]

$$\mathcal{T} : \mathcal{H}(\mathbf{k}) \rightarrow \sigma^y \mathcal{H}^*(-\mathbf{k})\sigma^y, \tag{1.24}$$

where * denotes complex conjugation. Physically, the time-reversal operation reverses the momentum, spin, and magnetic moment of all particles.

TR symmetry is closely connected to the stability of topological surface states. As mentioned above, insulators are classified by a topological invariant that takes different values for topological insulators than for ordinary insulators. The topological invariant is so-named because it is unchanged by any continuous modification of the Hamiltonian describing the system, provided that the energy gap of the system is not closed (i.e., the material remains insulating). Since the invariant does change across the interface between a topological and and ordinary insulator, one is forced to conclude that the two insulators are separated by a gapless (conducting) region. However, the invariants characterizing the quantum spin Hall state of Section 1.1 and three-dimensional TIs are only defined for systems that possess time-reversal symmetry. So breaking TR symmetry eliminates this particular mechanism for stabilization of the surface states, but Chapters 3 and 4 will present other stability mechanisms for related systems, that are in fact dependent on broken TR symmetry.

TR symmetry also has important implications for the transport of the surface electrons; scattering by non-magnetic impurities is suppressed because TR symmetry guarantees that for any possible scattering process, the reverse process has an opposite quantum amplitude,

so that there is no net contribution to the scattering probability. [21] However, magnetic impurities explicitly break TR symmetry by adding terms proportional to σ^x, σ^y, or σ^z (and even powers of $\mathbf{k}$), which change sign when acted upon by $\mathcal{T}$, so the above argument no longer holds. This breaking of TR symmetry will be essential for the results presented later in this thesis.

Chapter 2

Model System

The physical system modeled in this thesis consists of alternating thin layers of a three-dimensional strong topological insulator and a normal insulator, as described in [2, 3] and shown in Figure 2.1. As will be shown later in this section and in Section 2.2, this configuration results in another strong TI, but with the advantage that its energy gap, i.e., the mass of the Dirac fermions, can be tuned to a desired value by choosing appropriate thicknesses for the different layers. The semimetallic states of Chapters 3 and 4 both require a TR-breaking perturbation of a massive Dirac fermion, with the energy scale of the perturbation larger than the Dirac mass. This is made easier by tuning the Dirac mass to a small value, avoiding the need for very strong magnetic fields.

The z axis is taken to be perpendicular to the layers, while the x and y axes lie along the planes. The structure is periodic in the z direction, with period d. This system derives its electronic structure from the surface states of the individual TI layers, whose Hamiltonian is found by projecting the Hamiltonian (1.23) onto the x-y plane: [21]

$$\mathcal{H} = \sum_{\mathbf{k}_\perp} [\hbar v_F \tau^z (\hat{z} \times \boldsymbol{\sigma}) \cdot \mathbf{k}_\perp] c^\dagger_{\mathbf{k}_\perp} c_{\mathbf{k}_\perp}, \tag{2.1}$$

where $\mathbf{k}_\perp = k_x \hat{x} + k_y \hat{y}$ is the momentum perpendicular to the z axis, v_F is the Fermi velocity, $\boldsymbol{\sigma}$ and $\boldsymbol{\tau}$ are Pauli operators acting on the spin and surface (top or bottom) degrees of freedom, respectively, and $c^\dagger_{\mathbf{k}}$ and $c_{\mathbf{k}}$ are the creation and annihilation operators for electrons of momentum $\mathbf{k}$. The spin and surface indices are left implicit in the sum and the creation and annihilation operators for brevity.

In the layered configuration above, the different TI surfaces are coupled by the tunneling of electrons. This thesis will consider tunneling between opposite surfaces of a single TI
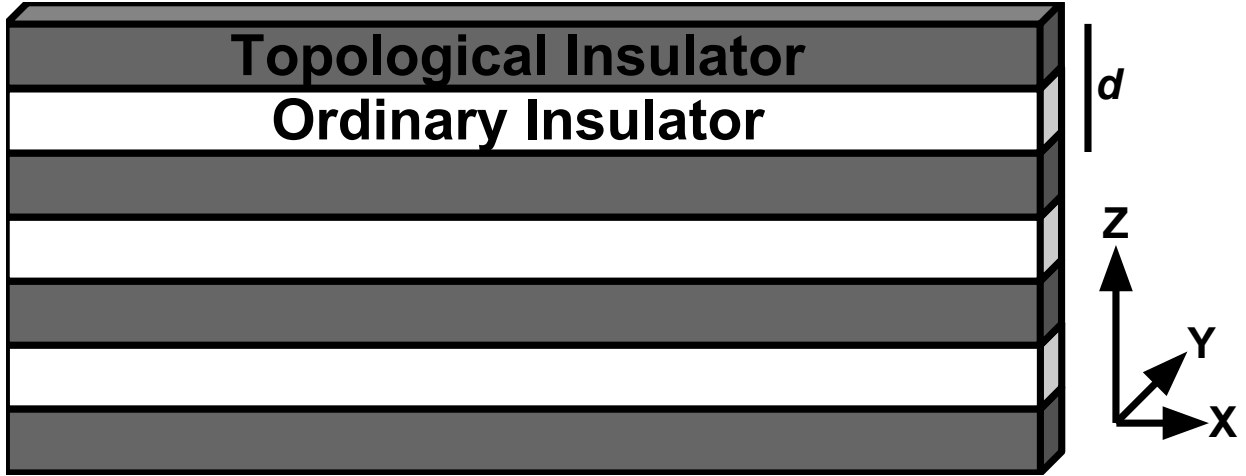
Figure 2.1: Structure of the TI multilayer system. Dark and light layers represent topological and ordinary insulators, respectively. Surface states described by Equation (2.1) are found at the boundaries between layers. Tunneling between layers gives rise to the Hamiltonian (2.2). The combined thickness of one topological insulator layer and one ordinary insulator layer is d.
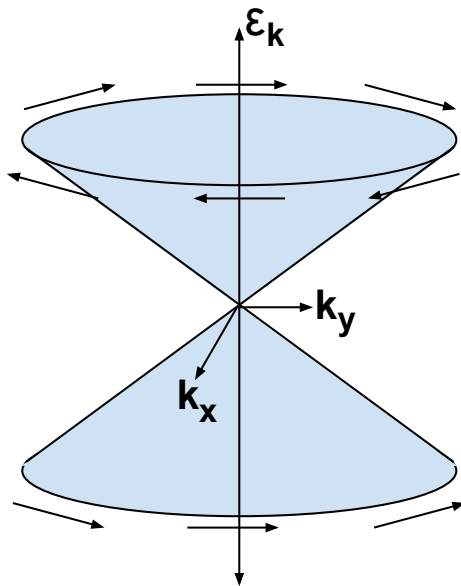
Figure 2.2: Surface energy states of a three-dimensional topological insulator with arrows representing spin. The band structure consists of a Dirac cone as in Figure 1.2, with an electron's spin always perpendicular to its momentum. Along a path in momentum space that encircles the Dirac point, the spins wind by 2π.

layer, and also tunneling across an ordinary insulator layer, between the top of one TI layer and the bottom of the TI layer above it. These processes are assigned tunneling amplitudes of Δ_S and Δ_D, respectively. The Hamiltonian of the multilayer system is then

$$\mathcal{H} = \sum_{\mathbf{k}_\perp, i, j} [\hbar v_F \tau^z (\hat{z} \times \boldsymbol{\sigma}) \cdot \mathbf{k}_\perp \delta_{i,j} + \Delta_S \tau^x \delta_{i,j} + \frac{1}{2} \Delta_D (\tau^+ \delta_{j,i+1} + \tau^- \delta_{j,i-1})] c^\dagger_{\mathbf{k}_\perp i} c_{\mathbf{k}_\perp j}, \quad (2.2)$$

where i and j run over each TI layer and $\tau^\pm = \tau^x \pm i\tau^y$. This Hamiltonian is in fact equivalent to (1.23) up to first order in $\mathbf{k}$ after transformations of $\boldsymbol{\sigma}$ and $\boldsymbol{\tau}$. Thus, this new system is also a three-dimensional strong TI, but with the gap tunable by choosing appropriate thicknesses for the different layers. Noting that $\sigma^y \sigma^x \sigma^y = -\sigma^x$ and $(\sigma^y)^* = -\sigma^y$, it can be verified that the Hamiltonians (2.1) and (2.2) are invariant the transformation (1.24), so this system possesses TR symmetry.

2.1 Single TI Layer

Before studying a many-layered system described by Equation (2.2), it is worth considering the case of a single TI layer, as in Ref. [27]. In this case, the Δ_D term and the summation over i and j are removed from Equation (2.2), giving

$$\mathcal{H} = \sum_{\mathbf{k}} [\hbar v_F \tau^z (\hat{z} \times \boldsymbol{\sigma}) \cdot \mathbf{k} + \Delta_S \tau^x] c^\dagger_{\mathbf{k}_\perp} c_{\mathbf{k}_\perp}, \quad (2.3)$$

where the subscript $\perp$ has been dropped from $\mathbf{k}$ for this section. Or, writing $\mathcal{H} = \sum_{\mathbf{k}_\perp} \mathcal{H}(\mathbf{k})$, and using the basis $\{| \uparrow, t\rangle, | \downarrow, t\rangle, | \uparrow, b\rangle, | \downarrow, b\rangle\}$, where the arrows represent spin and t and b stand for the top and bottom surfaces, $\mathcal{H}(\mathbf{k})$ can be represented by the 4x4 matrix

$$\mathcal{H}(\mathbf{k}) = \begin{pmatrix} 0 & \hbar v_F (ik_x + k_y) & \Delta_S & 0 \\ \hbar v_F (-ik_x + k_y) & 0 & 0 & \Delta_S \\ \Delta_S & 0 & 0 & \hbar v_F (-ik_x - k_y) \\ 0 & \Delta_S & \hbar v_F (ik_x - k_y) & 0 \end{pmatrix}. \quad (2.4)$$

This matrix is diagonalized to give the dispersion

$$|\epsilon_{\mathbf{k}}| = \sqrt{\hbar^2 v_F^2 \mathbf{k}^2 + \Delta_S^2}, \quad (2.5)$$

which is shown graphically in Figure 2.3(a). The tunneling term hybridizes the electronic states of the two surfaces, opening a gap and altering the topological nature of the material.
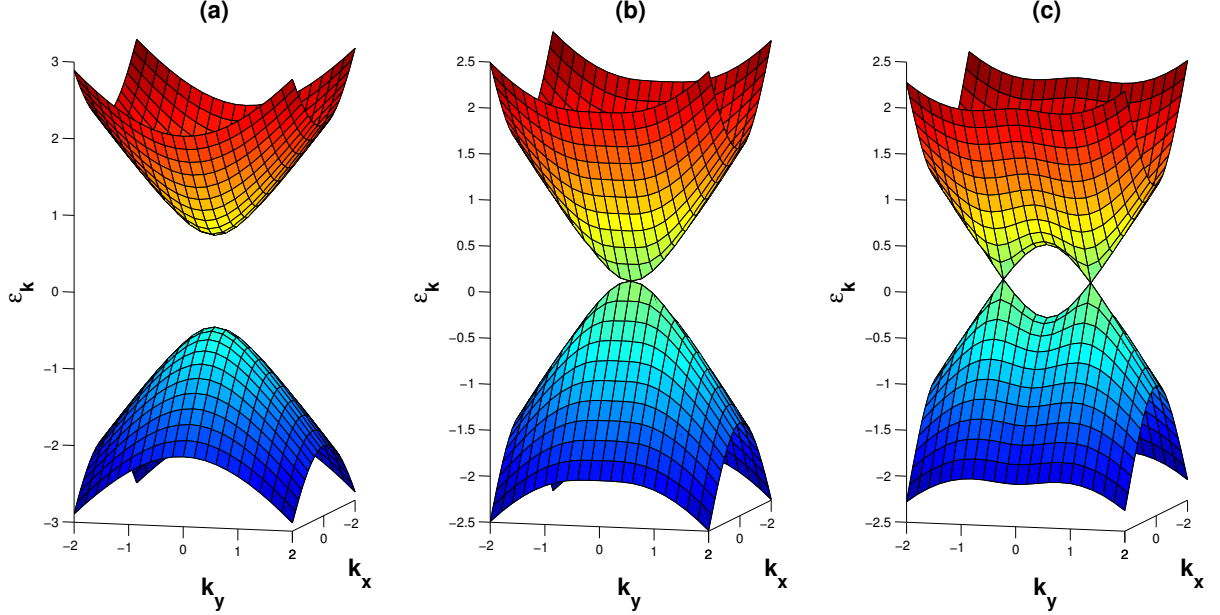
Figure 2.3: Band structure of a thin TI layer with tunneling between top and bottom surfaces and an applied in-plane magnetic field. The upper and lower bands are both doubly degenerate. (a) $b < |\Delta_S|$: The system is gapped. (b) $b = |\Delta_S|$: The gap closes at a single point in momentum space. (c) $b > |\Delta_S|$: The single node in (b) splits into two nodes separated in momentum space.

2.1.1 TR Symmetry-Breaking and Edge States

More interesting results are achieved upon breaking TR symmetry by adding a term $b\sigma^x$, corresponding to an applied magnetic field or ferromagnetic impurities with magnetic moments aligned in the x direction. In the case of an external field, the b term arises from a combination of two mechanisms as follows. First, there a term $\frac{g\mu_B}{2}B\sigma^x$ from the Zeeman coupling of the electron spins to the field, where $\mu_B = \frac{e\hbar}{2mc}$ is the Bohr magneton. In addition, the magnetic field influences the orbital motion of the electrons, an effect that can be represented by the transformation $\mathbf{k} \to \frac{e}{\hbar c}\mathbf{A}$, where $\mathbf{A} = -zB\hat{y}$ is the magnetic vector potential in the Landau gauge. Setting $z = \pm d_{\mathrm{TI}}/2$ for the top and bottom surfaces of the layer, respectively, the Hamiltonian can then be written as

$$\mathcal{H}(\mathbf{k}) = \hbar v_F \tau^z (\hat{z} \times \boldsymbol{\sigma}) \cdot \left(\mathbf{k} - \frac{eB}{\hbar c} \frac{d_{\mathrm{TI}}}{2} \tau^z \hat{y} \right) + \Delta_S \tau^x + \frac{ge\hbar}{4mc} B\sigma^x. \tag{2.6}$$

16

Expanding the dot product of $\hat{z} \times \sigma$ with the d_{TI} term gives

$$\mathcal{H}(\mathbf{k}) = \hbar v_F \tau^z (\hat{z} \times \boldsymbol{\sigma}) \cdot \mathbf{k} + \Delta_S \tau^x + \left(\frac{g\hbar^2}{4m\ell^2} - \frac{\hbar v_F d_{\text{TI}}}{2\ell^2} \right) \sigma^x, \tag{2.7}$$

where $\ell = \sqrt{\frac{\hbar c}{eB}}$ is the magnetic length.

So, defining $b = \left(\frac{g\hbar^2}{4m\ell^2} - \frac{\hbar v_F d_{\text{TI}}}{2\ell^2} \right)$, the Hamiltonian for the system with broken time-reversal symmetry is

$$\mathcal{H}(\mathbf{k}) = \hbar v_F \tau^z (\hat{z} \times \boldsymbol{\sigma}) \cdot \mathbf{k} + \Delta_S \tau^x + b\sigma^x, \tag{2.8}$$

with dispersion

$$|\epsilon_{\mathbf{k},\pm}| = \sqrt{\hbar^2 v_F^2 \mathbf{k}^2 + \Delta_S^2 + b^2 \pm 2b\sqrt{\hbar^2 v_F^2 k_y^2 + \Delta_S^2}}, \tag{2.9}$$

plotted in Figure 2.3. When $b \geq |\Delta_S|$, the gap closes again, with nodes located at $k_x = 0$, $k_y = \pm \frac{1}{\hbar v_F} \sqrt{b^2 - \Delta_S^2}$. Moreover, the system acquires a new topological character, with edge states that can be demonstrated by considering a sample limited to the $x \leq 0$ half-plane. Expanding Equation (2.3) and including the TR-breaking term above gives

$$\mathcal{H}(\mathbf{k}) = \hbar v_F k_y \tau^z \sigma^x - \hbar v_F k_x \tau^z \sigma^y + b\sigma^x + \Delta_S \tau^x. \tag{2.10}$$

The analysis is simplified by bringing the Hamiltonian to a block diagonal form, i.e. by transforming Equation (2.10) to eliminate all of the τ operators. To achieve this, first the spin quantization axis is rotated by $\frac{\pi}{2}$ around the y axis, so that $\sigma^x \to \sigma^z$ and $\sigma^z \to -\sigma^x$, giving

$$\mathcal{H}(\mathbf{k}) \to \hbar v_F k_y \tau^z \sigma^z - \hbar v_F k_x \tau^z \sigma^y + b\sigma^z + \Delta_S \tau^x. \tag{2.11}$$

This is followed by another transformation,

$$\sigma^{\pm} \to \tau^z \sigma^{\pm}, \ \tau^{\pm} \to \sigma^z \tau^{\pm}, \tag{2.12}$$

which gives

$$\mathcal{H}'(\mathbf{k}) = [\hbar v_F k_y \tau^z + b + \Delta_S \tau^x]\sigma^z - \hbar v_F k_x \sigma^y. \tag{2.13}$$

The factor in square brackets, $\hbar v_F k_y \tau^z + b + \Delta_S \tau^x$, commutes with $\mathcal{H}'$ since it contains only τ operators and real numbers, while the rest of $\mathcal{H}'$ contains only σ operators and real numbers. This means that it can be diagonalized simultaneously with $\mathcal{H}'$, and so it can be

replaced by its eigenvalues, $b \pm \sqrt{\hbar^2 v_F^2 k_y^2 + \Delta_S^2}$. This leads to two independent 2x2 blocks of the Hamiltonian,

$$\mathcal{H}'_{\pm}(\mathbf{k}) = (b \pm b_c)\sigma^z - \hbar v_F k_x \sigma^y, \tag{2.14}$$

where $b_c = \sqrt{\hbar^2 v_F^2 k_y^2 + \Delta_S^2}$. At this point, the edge states can be demonstrated in two ways, both of which will be presented here.

2.1.2 Topological Argument for Edge States

First, the presence of the edge states can be inferred from the topological properties of the the above Hamiltonian, specifically the $\mathcal{H}'_-$ block. In order to study the topology of the system, the Hamiltonian must be regularized to obtain a periodic function of k_x, as expected for a crystalline system. The particular form of the regularization is not important, provided that it reproduces Equation (2.14) when expanded to first order near $k_x = 0$ and does not create any additional nodes. To this end, one can use $k_x \to \sin(k_x)$ and $b \to \frac{b}{2}(1 + \cos(k_x))$, with the transformation of b accounting for the momentum-dependence of the electron g-factor.

For clarity, it is useful to imagine the Hamiltonian (2.14), with the above regularization, as describing a one dimensional system along the x axis, with k_y a parameter characterizing the system. To emphasize this, the regularized Hamiltonian can be written as

$$\mathcal{H}'_{k_y,-}(k_x) = \left[\frac{b}{2}(1 + \cos(k_x)) - b_c\right]\sigma^z - \hbar v_F \sin(k_x)\sigma^y. \tag{2.15}$$

Now one can consider the vector $\mathbf{g}(k_x) = -\hbar v_F \sin(k_x)\hat{y} + \left[\frac{b}{2}(1 + \cos(k_x)) - b_c\right]\hat{z}$, chosen to give $\mathbf{g}(k_x) \cdot \boldsymbol{\sigma} = \mathcal{H}'_-$. For $b < b_c$, g_z is negative for all k_x, whereas for $b > b_c$, one has $g_z > 0$ for k_x close to 0. As k_x traverses the first Brillouin zone, this sign change, combined with the sign change of $\sin(k_x)$ in the y component at $k_x = 0$, leads to a winding of $\mathbf{g}$ in the y-z plane for $b > b_c$ as shown in Figure 2.4. I.e., $\mathbf{g}$ has a winding number of 1 in this case. Provided that $\mathbf{g}$ does not acquire an x component (which is guaranteed in this case by certain discrete symmetries that will be discussed in Chapter 4), this winding number is topologically invariant; no continuous change in $\mathbf{g}$ can remove the winding without at some point causing $\mathbf{g}(k_x) = 0$ for some value of k_x. Since $\mathbf{g} \cdot \boldsymbol{\sigma} = \mathcal{H}'_-$, $\mathbf{g} = 0$ implies a closed energy gap.

The situation is now the same as that discussed in Section 1.4; for $b > b_c$, the winding number of $\mathbf{g}$ must change across the boundary at $x = 0$, since the vacuum has trivial topology. Thus, the energy gap for $|k_y| < \frac{1}{\hbar v_F}\sqrt{b^2 - \Delta_S^2}$ must close along the $x = 0$ edge, as shown in Figure 2.5.

18
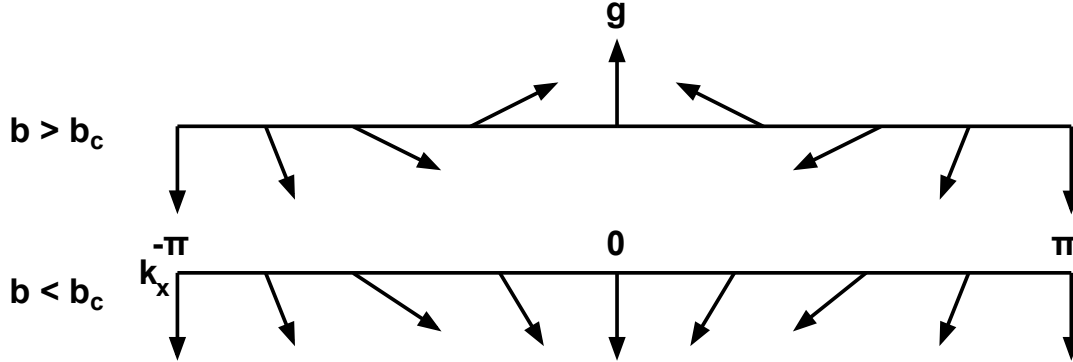
Figure 2.4: Illustration of the winding of the vector **g**, defined so that the Hamiltonian is **g** · **σ**, as a function of k_x in the first Brillouin zone. For $b > b_c$, meaning that k_y is between the two nodes, **g** winds counterclockwise once as k_x traverses the first Brillouin zone. For $b < b_c$, k_y is not between the nodes (if any) and there is no winding of **g**.

2.1.3   Explicit Calculation of Edge State Wavefunctions

The edge states can be demonstrated explicitly by seeking zero energy states, using a real space rather than momentum space description in the x direction: $k_x \to -i\partial/\partial x$. For $b > 0$, only $\mathcal{H}_-$ is relevant to the edge states, which therefore must satisfy

$$[b(x) - b_c]\sigma^z \Psi(x) + i\hbar v_F \sigma^y \frac{\partial \Psi}{\partial x} = 0, \tag{2.16}$$

where Ψ is a two-component spinor, and the field b is now assumed to have position dependence with $b(x) \to 0$ as $x \to \infty$ (i.e., the field is zero far from the sample). This can be simplified by assuming a solution of the form $\Psi(x) = i\sigma^y e^{F(x)}\phi$, with ϕ a position-independent spinor, leading to the new equation

$$[b(x) - b_c]\sigma^x \phi = \hbar v_F \frac{dF}{dx}\phi. \tag{2.17}$$

A normalizable solution to (2.16) requires that $F(x) \to -\infty$ as $x \to \pm\infty$, meaning that $\frac{dF}{dx}$, and hence $b(x) - b_c$ also, must have opposite signs as $x \to \pm\infty$. Thus, zero energy states occur only if $b > b_c$ inside the sample, in which case the solution is given by

$$\Psi(x) = e^{\frac{1}{\hbar v_F} \int_0^x dx' [b(x') - b_c]} |\sigma^x = -1\rangle. \tag{2.18}$$

19
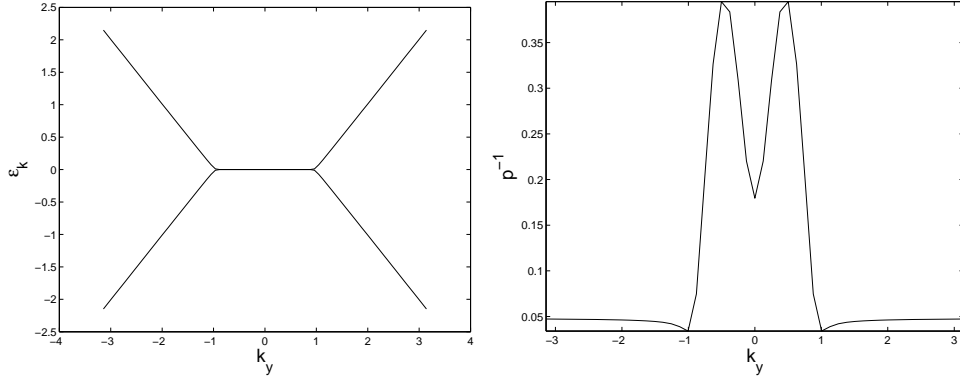
Figure 2.5: Left: energy spectrum of a thin TI film with an in-plane magnetic field and finite size along the x direction, showing the dispersionless states on the $x = 0$ edge. Right: Inverse participation ratio for the same system, showing that electronic wavefunctions in the interval of the flat dispersion are indeed localized to the edge.

As expected, these zero energy states are localized to the edge of the sample at $x = 0$.

The edge state dispersion and wavefunctions can also be calculated numerically to verify the above result. The regularized Hamiltonian 2.15 is converted to a description in terms of N discrete positions along the x axis by a Fourier transform:

$$c_{k_x}^\dagger = \frac{1}{\sqrt{N}} \sum_{k_x} c_j^\dagger e^{ik_x j}, \tag{2.19}$$

so

$$\mathcal{H}'_{k_y,-}(j) = \frac{1}{N} \sum_{k_x,j,j'} \left(\left[\frac{b}{2}(1 + \cos(k_x)) - b_c \right] \sigma^z - \hbar v_F \sin(k_x)\sigma^y \right) e^{-ik_x(j'-j)} c_j^\dagger c_{j'}. \tag{2.20}$$

Using the identity $\frac{1}{N} \sum_k e^{ik(j'-j)} = \delta_{j,j'}$, the Hamiltonian simplifies to

$$\mathcal{H}'_{k_y,-}(j) = \sum_j \left(\frac{b}{2} - b_c \right) \sigma^z c_j^\dagger c_j + \sum_j \left(\frac{b}{4}\sigma^z + \frac{i\hbar v_F \sigma^y}{2}\sigma^x \right) c_j^\dagger c_{j+1} +$$

$$+ \sum_j \left(\frac{b}{4}\sigma^z + \frac{-i\hbar v_F \sigma^y}{2}\sigma^x \right) c_j^\dagger c_{j-1}, \tag{2.21}$$

for which the electron energies can be calculated numerically, with the results shown in Figure 2.5, confirming the presence of gapless surface states between the point nodes.

20

A participation ratio can also be defined from the eigenstates of (2.21) to characterize the degree to which the wavefunctions are localized at the edge. For a normalized wavefunction $\psi_{k_y}(j, \sigma)$, the inverse participation ratio is defined as

$$p_{\psi_{k_y}}^{-1} = \sum_j P_j(\psi_{k_y})^2, \tag{2.22}$$

where $P_j(\psi_{k_y}) = |\psi_{k_y}(j, \sigma)|^2 + |\psi_{k_y}(j, -\sigma)|^2$ is the probability for an electron with momentum k_y to be found at position j. For a wavefunction localized at a single point in space, $p_\psi^{-1} = 1$, while for a uniformly distributed state, $p_\psi^{-1} = 1/N$, so a larger value of p_ψ^{-1} suggests a wavefunction that is more strongly localized.

2.1.4 Magnetic Susceptibility

One physical consequence of the transition between the gapped state with $b < |\Delta_S|$ and the gapless state $b \geq |\Delta_S|$ is found by computing the magnetic susceptibility of the system at zero temperature, given by the differentiating the free energy twice with respect to the applied field. In general, the free energy (grand potential) at a temperature T and chemical potential μ is

$$F = -k_B T \ln \left(\prod_i \sum_{n_i} e^{-n_i(\epsilon_i - \mu)/k_B T} \right), \tag{2.23}$$

where i runs over all eigenstates of the Hamiltonian, ϵ_i is the energy of eigenstate i, and k_B is the Boltzmann constant. For fermions, each n_i can only be 0 or 1, and for this system, there are four energy eigenvalues for each momentum $\mathbf{k}$, given by Equation (2.9). The free energy is therefore

$$F = -k_B T \sum_{\mathbf{k}} \left[\ln \left(1 + e^{-\frac{\epsilon_{\mathbf{k},+} - \mu}{k_B T}} \right) + \ln \left(1 + e^{-\frac{\epsilon_{\mathbf{k},-} - \mu}{k_B T}} \right) \right.$$
$$\left. + \ln \left(1 + e^{\frac{\epsilon_{\mathbf{k},+} + \mu}{k_B T}} \right) + \ln \left(1 + e^{\frac{\epsilon_{\mathbf{k},-} + \mu}{k_B T}} \right) \right]. \tag{2.24}$$

The susceptibility is then

$$\chi(B) = -\frac{1}{d_{\mathrm{TI}} A} \frac{\partial^2 F}{\partial B^2}, \tag{2.25}$$

where d_{TI} is the thickness of the TI layer and A is its area. Computing this expression explicitly for $\mu = 0$, one first obtains

$$\frac{\partial F}{\partial B} = -k_B T \frac{db}{dB} \sum_{\mathbf{k}} \left(\frac{\sinh(\tilde{\epsilon}_{\mathbf{k},+})}{1 + \cosh(\tilde{\epsilon}_{\mathbf{k},+})} \frac{\partial \tilde{\epsilon}_{\mathbf{k},+}}{\partial B} + \frac{\sinh(\tilde{\epsilon}_{\mathbf{k},-})}{1 + \cosh(\tilde{\epsilon}_{\mathbf{k},-})} \frac{\partial \tilde{\epsilon}_{\mathbf{k},-}}{\partial B} \right), \tag{2.26}$$

21

where $\tilde{\epsilon}_{k,\pm} = \epsilon_{k,\pm}/k_B T$. In the limit $T \to 0$, $\tilde{\epsilon}_{k,\pm} \to \infty$, except at the nodes, which do not contribute significantly to the sum, so $\frac{\sinh(\tilde{\epsilon}_{\mathbf{k},+})}{1+\cosh(\tilde{\epsilon}_{\mathbf{k},+})} \to 1$. Differentiating again yields

$$\frac{\partial^2 F}{\partial B^2} = -k_B T \left(\frac{db}{dB}\right)^2 \sum_{\mathbf{k}} \left[\frac{\partial^2 \tilde{\epsilon}_{\mathbf{k},+}}{\partial b^2} + \frac{\partial^2 \tilde{\epsilon}_{\mathbf{k},-}}{\partial b^2}\right]$$

$$= -\left(\frac{db}{dB}\right)^2 \sum_{\mathbf{k}} \hbar^2 v_F^2 k_x^2 \left(\frac{1}{\epsilon_{\mathbf{k},+}^3} + \frac{1}{\epsilon_{\mathbf{k},-}^3}\right). \tag{2.27}$$

However, this expression is divergent for large k_x. This divergence is eliminated by subtracting the susceptibility for $\Delta_S = 0$, which is zero for physical reasons.[27] Assuming the sample is large in area, the sum over $\mathbf{k}$ can be replaced by an integral, giving

$$\chi(B) = A \left(\frac{db}{dB}\right)^2 \mathcal{I}(B), \tag{2.28}$$

where

$$\mathcal{I}(B) = \int \frac{d^2 k}{4\pi^2} \hbar^2 v_F^2 k_x^2 \left[\frac{1}{\epsilon_{\mathbf{k},+}^3} + \frac{1}{\epsilon_{\mathbf{k},-}^3} - \frac{1}{\epsilon_{\mathbf{k},+}^3}\bigg|_{\Delta_S=0} - \frac{1}{\epsilon_{\mathbf{k},-}^3}\bigg|_{\Delta_S=0}\right]. \tag{2.29}$$

This integral can be evaluated directly, beginning with the integral over k_x, giving

$$\mathcal{I}(B) = \frac{1}{2\pi^2 v_F} \int_{-\infty}^{\infty} dk_y \ln \left|\frac{k_y^2 - \left(\frac{b}{v_F}\right)^2}{k_y^2 - k_0^2}\right|, \tag{2.30}$$

where $k_0 = (1/v_F)\sqrt{b^2 - \Delta_S^2}$ is real and gives the position of the nodes along the k_y axis when $b \geq |\Delta_S|$, but is imaginary when $b < |\Delta_S|$. When k_0 is real, the integrand can be rewritten as

$$\ln \left|\frac{\tilde{k}_y - 1}{\tilde{k}_y - \tilde{k}_0}\right| + \ln \left|\frac{\tilde{k}_y + 1}{\tilde{k}_y + \tilde{k}_0}\right|, \tag{2.31}$$

where $\tilde{k}_y = \frac{\hbar v_F k_y}{b}$ and $\tilde{k}_0 = \frac{k_0}{b}$. The logarithms above are odd under the reflections $\tilde{k}_y \to -\tilde{k}_y + (1 + \tilde{k}_0)$ and $\tilde{k}_y \to -\tilde{k}_y - (1 + \tilde{k}_0)$, respectively, so their integrals must be zero.

22
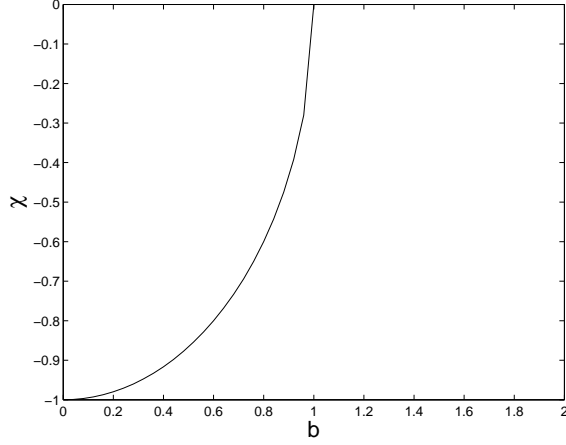
Figure 2.6: Magnetic susceptibility of a thin TI film subject to an in-plane magnetic field, plotted as a function of the field (shown for $\Delta_S = 1$).

When $|\Delta_S| > b$, k_0 is imaginary, and (2.30) can be evaluated directly as

$$
\mathcal{I}(B) = \frac{1}{2\pi^2 v_F} \left[\tilde{k}_y \ln \left| \frac{\tilde{k}_y^2 - 1}{\tilde{k}_y^2 + \tilde{\Delta}_S^2 - 1} \right| + \ln \left| \frac{\tilde{k}_y + 1}{\tilde{k}_y - 1} \right| - 2\sqrt{\tilde{\Delta}_S^2 - 1} \arctan \left(\frac{\tilde{k}_y}{\sqrt{\tilde{\Delta}_S^2 - 1}} \right) \right]_{-\infty}^{\infty}
$$
$$
= \frac{-1}{\pi v_F^2} \sqrt{\Delta_S^2 - b^2}. \tag{2.32}
$$

Therefore the susceptibility is

$$
\chi(B) = \begin{cases} 0 & \text{if } b \geq \Delta_S \\ \frac{-e^2 B}{\pi v_F^2 c^2} \left(\frac{g\hbar}{4m} - \frac{v_F d_{\text{TI}}}{2} \right)^2 \sqrt{\Delta_S^2 - b^2} & \text{if } b < \Delta_S. \end{cases} \tag{2.33}
$$

2.2 Ordinary Insulator to Topological Insulator Transition

Returning to the many-layered system, it is useful to transform from the description in terms of tunneling between discrete layers, found in Equation (2.2), to one in terms of the

23

momenta of electrons along the z axis. Substituting the Fourier transform

$$c^\dagger_{\mathbf{k}_\perp, j} = \frac{1}{\sqrt{N}} \sum_{k_z} c^\dagger_{\mathbf{k}} e^{-ik_z dj}, \tag{2.34}$$

where N is the number of TI layers, into (2.2) gives the momentum-space Hamiltonian

$$\mathcal{H} = \sum_{\mathbf{k}} \left[\hbar v_F \tau^z \left(\hat{z} \times \boldsymbol{\sigma} \right) \cdot \mathbf{k} + \hat{\Delta}(k_z) \right] c^\dagger_{\mathbf{k}} c_{\mathbf{k}}, \tag{2.35}$$

where $\hat{\Delta}(k_z) = \Delta_S \tau^x + \frac{1}{2}\Delta_D \left(\tau^+ e^{ik_z d} + \tau^- e^{-ik_z d} \right)$. Assuming that the sample has a length L along the z axis, the allowed values of k_z are $2\pi n/L$, where n is an integer. This Hamiltonian has two doubly degenerate bands given by

$$\epsilon_\pm(\mathbf{k}) = \pm\sqrt{\hbar^2 v_F^2(k_x^2 + k_y^2) + \Delta_S^2 + \Delta_D^2 + 2\Delta_S\Delta_D \cos(k_z d)}. \tag{2.36}$$

A key property of this system is the band-touching that occurs when $|\Delta_S| = |\Delta_D|$. The location of the band-touching in momentum space depends on the relative signs of Δ_S and Δ_D; in the case $\Delta_S, \Delta_D > 0$, the node is located at $k_x = k_y = 0, k_z = \pi/d$. Since $\mathcal{H}(\mathbf{k})$ is periodic in k_z, with period $2\pi/d$, k_z will be chosen to lie in the interval $[0, 2\pi/d]$ so that the node is located at the centre of the range of k_z.

Approximating the Hamiltonian for momenta close to the node gives

$$\mathcal{H}(\mathbf{k}) = \hbar v_F \tau^z (\hat{z} \times \boldsymbol{\sigma}) \cdot \mathbf{k} + \Delta_D \tau^y \left(k_z - \frac{\pi}{d} \right) d + (\Delta_S - \Delta_D)\tau^x. \tag{2.37}$$

This equation has the same form as that of a general four-component Dirac fermion as discussed in Section 1.2 with the gamma matrices given by equation 1.19:

$$\gamma_1 = -\tau^z \sigma^y, \quad \gamma_2 = \tau^z \sigma^x, \quad \gamma_3 = \tau^y, \quad \gamma_4 = \tau^x, \text{ and } \gamma_5 = \tau^z \sigma^z. \tag{2.38}$$

The mass of the Dirac fermion is therefore $\Delta_S - \Delta_D$; the mass is zero when $\Delta_S = \Delta_D$ and changes sign depending on the relative magnitudes of Δ_S and Δ_D. As discussed in Section 1.2, this sign change implies a transition between different topologies, with the state $\Delta_S > \Delta_D$ having trivial topology, since the limit $\Delta_S/\Delta_D \to \infty$ corresponds to a structure composed entirely of ordinary insulator layers, with the TI layers having vanishing thickness in comparison. Breaking time-reversal symmetry near the transition point produces the Weyl semimetal phase of Chapter 3 or the line node semimetal of Chapter 4, depending on the particular mechanism of TR symmetry-breaking.

Chapter 3

Weyl Semimetal

This chapter examines the effect of adding a term $b\sigma^z$ to the Hamiltonian (2.35), the momentum-space description of the multilayer heterostructure introduced in Chapter 2. This term can be generated by doping the material with ferromagnetic impurities with their magnetic moments aligned along the z axis. With this addition, the Hamiltonian becomes

$$\mathcal{H}(\mathbf{k}) = \hbar v_F \tau^z (\hat{z} \times \boldsymbol{\sigma}) \cdot \mathbf{k} + b\sigma^z + \hat{\Delta}(k_z),$$ (3.1)

where $\hat{\Delta}(k_z) = \Delta_s \tau^x + \frac{1}{2}\Delta_D \left(\tau^+ e^{ik_z d} + \tau^- e^{-ik_z d} \right)$. The energy eigenvalues are

$$|\epsilon_{\mathbf{k},\pm}| = \sqrt{\hbar^2 v_F^2 (k_x^2 + k_y^2) + \left[b \pm \sqrt{\Delta_S^2 + \Delta_D^2 + 2\Delta_S \Delta_D \cos(k_z d)} \right]^2}.$$ (3.2)

For b between $m_{c1} = |\Delta_S - \Delta_D|$ and $m_{c2} = \Delta_S + \Delta_D$, there are two point nodes for which $\epsilon_{\mathbf{k},-} = 0$. The $\epsilon_{\mathbf{k},-}$ bands for this case are plotted in Figure 3.1, showing two nodes along the k_z axis, located at $k_z = \pi/d \pm k_0$, where $k_0 = \frac{1}{d}\arccos[1 - (b^2 - (\Delta_S - \Delta_D)^2)/2\Delta_S \Delta_D]$. This state is the topological Weyl semimetal described in [2] and [3]. It has also been predicted to occur in iridium compounds on pyrochlore lattices,[24, 26] but these systems are much more complicated than the version described here, having 24 Weyl nodes instead of two, the smallest possible number since Weyl nodes always appear in pairs with opposite chiralities.

To study this state in detail, it is useful to make the transformation $\sigma^\pm \to \tau^z \sigma^\pm$, $\tau^\pm \to \sigma^z \tau^\pm$, giving

$$\mathcal{H}(\mathbf{k}) = \hbar v_F (k_y \sigma^x - k_x \sigma^y) + [b + \hat{\Delta}(k_z)]\sigma^z.$$ (3.3)
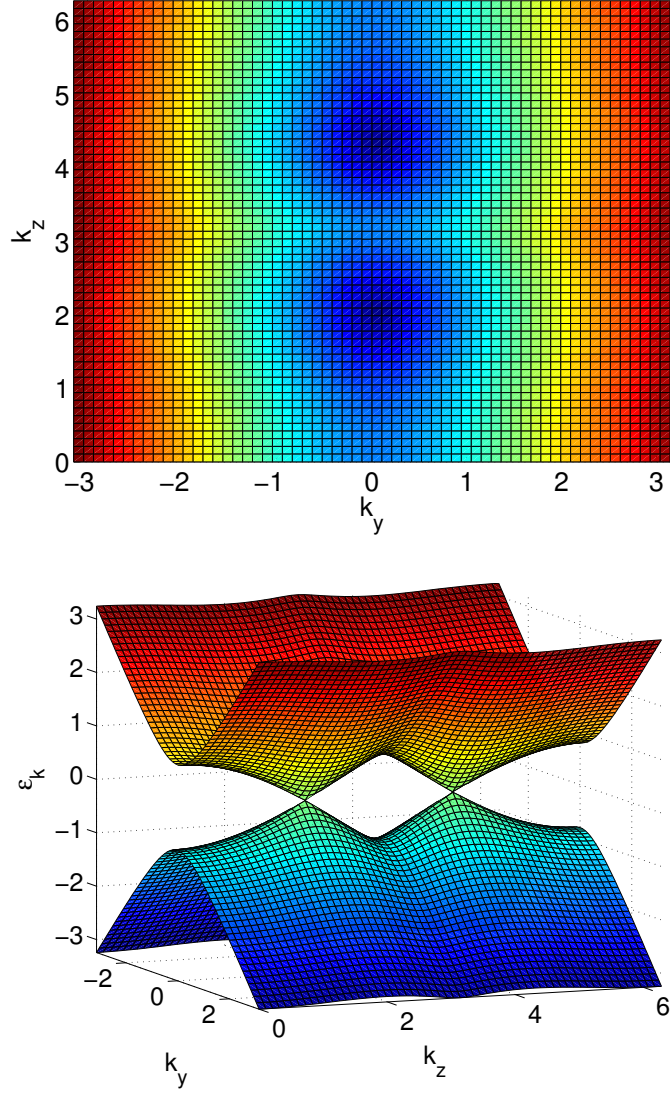
Figure 3.1: Plots of the bulk electronic dispersion of the Weyl semimetal. There are two Weyl nodes, located at $k_x = k_y = 0, k_z = \pi/d \pm k_0$, with k_0 given in the text. At these points, the energy gap closes and the electronic dispersion is linear. These Weyl nodes are stable due to their separation in momentum space: they can only be eliminated by closing the separation between them, allowing the two Weyl nodes of opposite chirality to eliminate each other.

Since $\hat{\Delta}(k_z)$ contains only τ operators, it commutes with $\mathcal{H}(\mathbf{k})$, and can be replaced by its eigenvalues, giving

$$\mathcal{H}_{\pm}(\mathbf{k}) = \hbar v_F(k_y\sigma^x - k_x\sigma^y) + [b \pm \Delta(k_z)]\sigma^z, \tag{3.4}$$

where $\Delta(k_z) = \sqrt{\Delta_S^2 + \Delta_D^2 + 2\Delta_S\Delta_D\cos(k_zd)}$. Focusing on the $-\Delta(k_z)$ eigenvalue, the lower band of the Hamiltonian can be approximated to first order as

$$\mathcal{H}_{\pm}(\mathbf{k}) = \hbar v_F(k_y\sigma^x - k_x\sigma^y) \pm \hbar v_z k_z\sigma^z, \tag{3.5}$$

where $v_z = \frac{\Delta_S\Delta_D d\sin(k_0d)}{b\hbar}$. Rescaling the momenta and rotating the pseudospins by $\pi/2$ about the z axis (i.e., applying the unitary operations $\mathcal{H}_{\pm} \to U_{\pm}^{\dagger}\mathcal{H}_{\pm}U_{\pm}$, where $U_{\pm}$ are the rotation operators $R_z(\mp\pi/2) = \exp(\pm i\pi\sigma^z/4)$) gives

$$\mathcal{H}_{\pm} = \pm(k_x\sigma^x + k_y\sigma^y + k_z\sigma^z), \tag{3.6}$$

demonstrating the connection to the generic Weyl decomposition of Equation (1.22). There are two Weyl nodes of opposite chirality separated in momentum space by $2k_0$ along the k_z axis. The individual Weyl nodes are stable in the presence of any possible perturbation: any operator acting on a 2×2 Hilbert space can be written in the form $\mathcal{H}_p = a_0 + a_x\sigma^x + a_y\sigma^y + a_z\sigma^z$. Added to Equation (3.6), this perturbation gives the new Hamiltonian

$$\mathcal{H}_{\pm} = a_0 \pm [(k_x \pm a_x)\sigma^x + (k_y \pm a_y)\sigma^y + (k_z \pm a_z)\sigma^z)], \tag{3.7}$$

which still describes a Weyl fermion. The Weyl fermion has been translated in momentum space and in energy, but these transformations have no physical significance, since the addition of a constant energy has no effect, while a translation in momentum space corresponds to a change to another inertial reference frame, again having no effect in the case of a translationally invariant system. Thus, the Weyl nodes can only be eliminated by removing the separation in momentum space space, allowing the Weyl nodes with opposite chiralities to become coupled, creating a mass and corresponding energy gap as in Equation (1.22).

Like the single-layered system of Section 2.1, the Weyl semimetal also has gapless topological surface states. In this case, they occur along any surface not normal to the z axis, for values of k_z lying between the Weyl nodes. Their wavefunctions can be calculated explicitly using a method similar to that of Section 2.1.3. For a semi-infinite system in the region $y < 0$, the Hamiltonian (3.4) has surface state solutions given by [2]:

$$\psi_{\text{surf}} = e^{\int_0^y dy'\, b(y') - \Delta(k_z)]/\hbar v_F}|\sigma^y = -1\rangle, \tag{3.8}$$

with energies $\epsilon_{\text{surf}} = \hbar v_F k_x$. The energy bands for a sample that is finite in the y direction are shown in Figure 3.2.
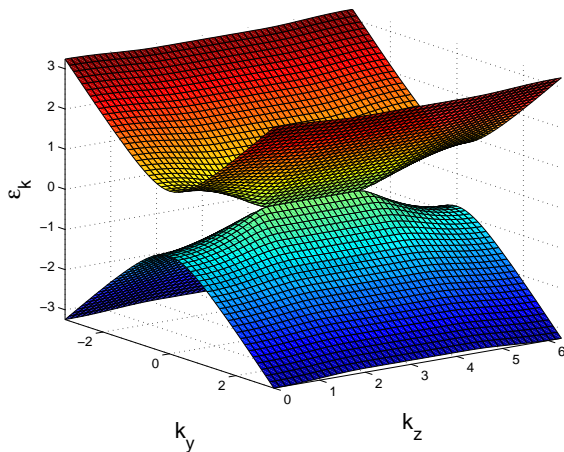
Figure 3.2: Band structure of a Weyl semimetal that is finite in the y direction, showing the line of zero-energy states on the surface.

3.1 Hall Conductivity

A key physically measurable property of the Weyl semimetal is its Hall conductivity, which can be computed by treating the Hamiltonian of Equation (3.4) as a set of two-dimensional Dirac fermions in the x-y plane, each with a Dirac mass parameterized by k_z as $b + \Delta(k_z)$.[2] This Dirac mass changes sign at the Weyl nodes, with $b - \Delta(k_z) > 0$ for $|\pi/d - k_z| < k_0$ and $b - \Delta(k_z) < 0$ for $|\pi/d - k_z| > k_0$, as shown in Figure 3.3. This change in the sign of the mass corresponds to a quantum Hall transition, which will be described more fully in Section 3.3, and means that 2-D systems with $|\pi/d - k_z| < k_0$ contribute a Hall conductance e^2/h. I.e., as a function of k_z, the two-dimensional Hall conductance is

$$\sigma_{xy}^{2\mathrm{D}}(k_z) = \begin{cases} 0 & \text{if } |\frac{\pi}{d} - k_z| > k_0 \\ e^2/h & \text{if } |\frac{\pi}{d} - k_z| < k_0. \end{cases} \tag{3.9}$$

The Hall conductivity of the three-dimensional system is therefore

$$\sigma_{xy} = \frac{1}{L} \sum_{k_z} \sigma_{xy}^{2\mathrm{D}}(k_z), \tag{3.10}$$

where L is the height of the sample. For an infinitely tall sample, the sum over k_z is

28
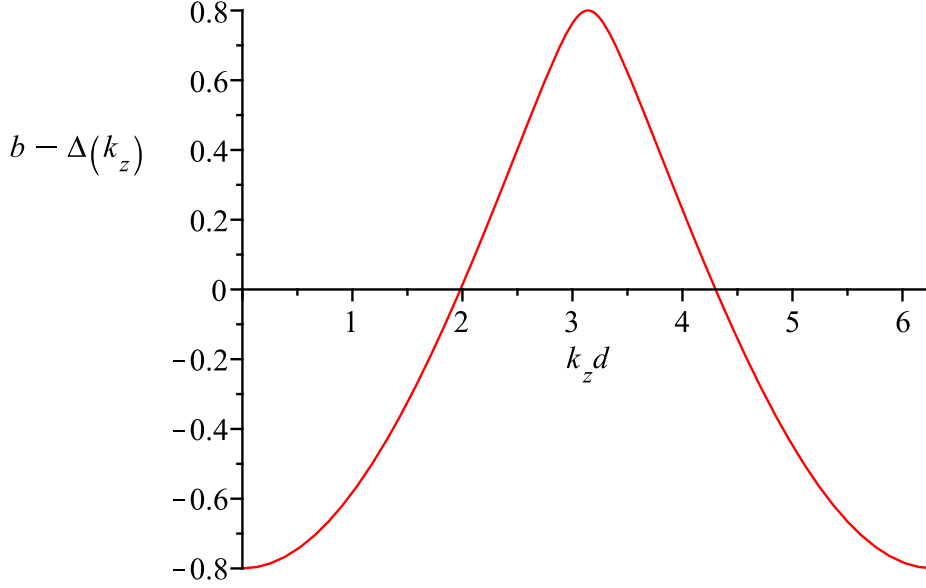
Figure 3.3: Plot of the Dirac mass $b - \Delta(k_z)$ as a function of k_z. The mass is positive between the Weyl nodes, which are located at $\pm k_0$.

rewritten as an integral:

$$\sigma_{xy} = \int_{\pi/d-k_0}^{\pi/d+k_0} \frac{\mathrm{d}k_z}{2\pi} \sigma_{xy}^{2\mathrm{D}}(k_z)$$
$$= \frac{e^2 k_0}{\pi h}. \tag{3.11}$$

So the Hall conductivity is directly proportional to the separation between the Weyl nodes, and is independent of all other material parameters. For a finite system, the Hall conductivity (as a function of b) displays a series of discrete jumps, each occurring when k_0 crosses one of the allowed values of k_z, which are given by $k_z = 2\pi n/L$, with n an integer. Between the jumps, σ_{xy} is constant. The Hall conductivities for finite and infinite samples are shown in Figure 3.4.
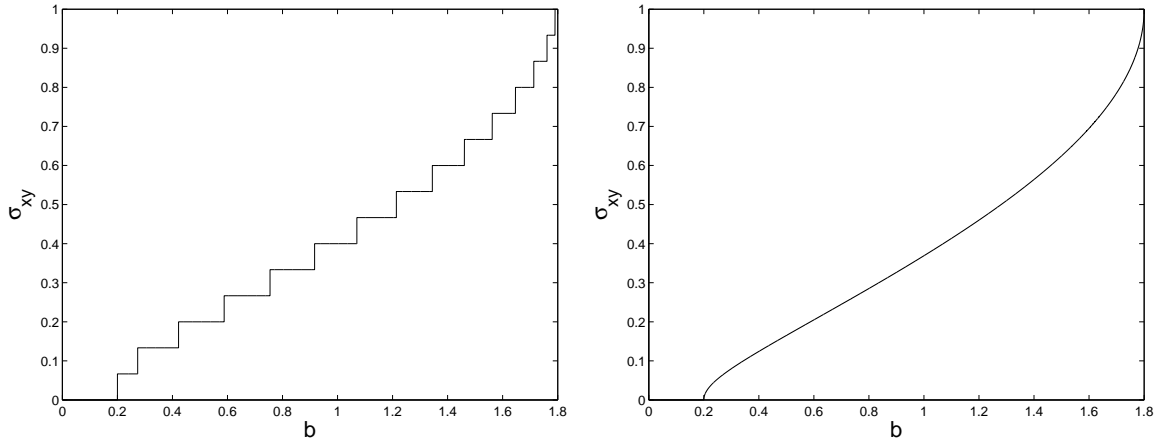
Figure 3.4: Hall conductivity (in units of e^2/dh) of the Weyl semimetal, plotted as a function of the TR-breaking field for a system with 30 TI layers (left) and an infinite number of layers (right), with $\Delta_S = 1$, $\Delta_D = 0.8$. The Weyl semimetal phase occurs for $|\Delta_S - \Delta_D| < b < \Delta_S + \Delta_D$, with the Hall conductivity proportional to the number of momentum states between the Weyl nodes; jumps in the finite-size Hall conductivity occur when a Weyl node crosses one of the discrete values of k_z that are allowed: $k_z = 2\pi n/L$ for an integer n.
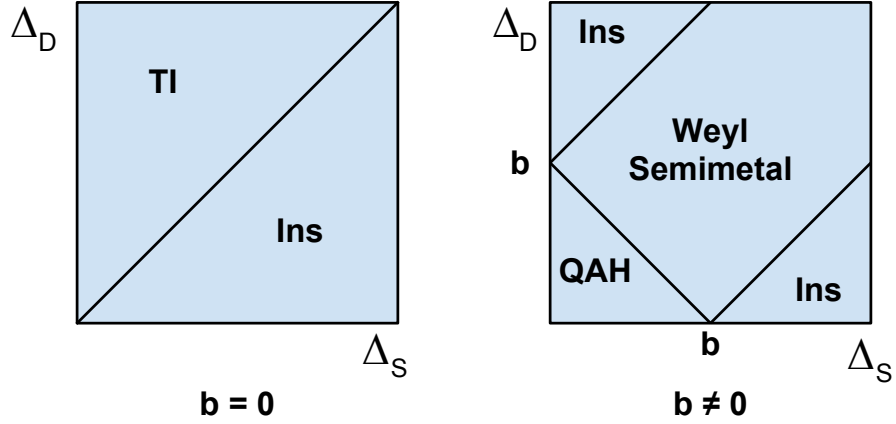
Figure 3.5: Phase diagram of the multilayer system with spin-splitting b due to ferromagnetic impurities with magnetic moments aligned along the z axis. For $b = 0$ (left), there is a topological insulator phase for $\Delta_D > \Delta_S$; otherwise the material is a normal insulator. For $b \neq 0$ (right), there is a Weyl semimetal phase when $|\Delta_S - \Delta_D| < b < \Delta_S + \Delta_D$, a quantum anomalous Hall phase when $b > \Delta_S + \Delta_D$, and a normal insulator when $b < |\Delta_S - \Delta_D|$.

3.2   Quantum Anomalous Hall Insulator

As the spin splitting b increases, the spacing between the Weyl nodes, $2k_0$, increases. However, the model system consists of discrete layers alternating between topological and ordinary insulator layers. The discreteness of these layers means that k_z must be periodic, with any two points in momentum space separated by $2\pi/d$ along the k_z axis being equivalent. So in addition to the Weyl nodes at $k_z = \pi/d \pm k_0$, there are equivalent Weyl nodes at $k_z = (2n + 1)\pi/d \pm k_0$ for any integer n. When $b = \Delta_S + \Delta_D$, $k_0 = \pi/d$, so that Weyl nodes of opposite chirality from adjacent copies of the Brillouin zone meet and annihilate each other, leaving a gapped energy spectrum, as is the case with spin splitting that is insufficient to counter the energy gap created by tunneling, described in Section 2.2. However, the new system is topologically distinct, retaining a non-zero Hall conductivity $\sigma_{xy} = e^2/dh$, the maximal value of the Hall conductivity of the Weyl semimetal.

3.3 Externally Applied Magnetic Field

Previously in this chapter, the spin-splitting necessary for the Weyl semimetal was assumed to be generated by doping the material with ferromagnetic impurities. Experimentally, it is simpler to achieve the spin-splitting by applying an external magnetic field perpendicular to the layers of the material (along the z axis).

The mathematical description begins with the Hamiltonian (2.35):

$$\mathcal{H}(\mathbf{k}) = \hbar v_F \tau^z \left(\hat{z} \times \boldsymbol{\sigma} \right) \cdot \mathbf{k} + \hat{\Delta}(k_z). \tag{3.12}$$

Like the ferromagnetic impurities, the magnetic field generates a spin-splitting term σ^z, but it also has an effect on the orbital motion of the electrons due to the Lorentz force. This additional effect is taken into account by replacing $\mathbf{k}$ with $-i\nabla + \frac{e}{\hbar c}\mathbf{A}$, where $\mathbf{A}$ is the magnetic vector potential. For a magnetic field $\mathbf{B} = B\hat{z}$, the vector potential can be chosen as $\mathbf{A} = xB\hat{y}$, which is known as the Landau gauge. Since the vector potential is independent of z, the momentum space form of the tunneling term can be retained, and the Hamiltonian is

$$\mathcal{H} = \hbar v_F \tau^z (\hat{z} \times \sigma) \cdot \left(-i\nabla + \frac{e}{\hbar c}\mathbf{A} \right) + \frac{g\mu_B}{2}B\sigma^z + \hat{\Delta}(k_z), \tag{3.13}$$

where g is a material parameter ($g \approx 50$ for BI_2Se_3, for example [3]) and μ_B is the Bohr magneton. Using the transformation $\sigma^\pm \to \tau^z \sigma^\pm$, $\tau^\pm \to \sigma^z \tau^\pm$ as in (2.12) and diagonalizing the tunneling term gives

$$\mathcal{H}_\pm = \hbar v_F (\hat{z} \times \sigma) \cdot \left(-i\nabla + \frac{e}{c}\mathbf{A} \right) + m_\pm(k_z)\sigma^z, \tag{3.14}$$

where $m_\pm(k_z) = b \pm \Delta(k_z)$ and $b = g\mu_B B/2$. Expanding the cross and dot products:

$$\mathcal{H}_\pm = \hbar v_F \left(-i\frac{\partial}{\partial y} + \frac{eB}{\hbar c}x \right) \sigma^x + i\hbar v_F \frac{\partial}{\partial x}\sigma^y + m_\pm(k_z)\sigma^z. \tag{3.15}$$

Defining $\ell = \sqrt{\frac{\hbar c}{eB}}$ and rotating the spin operators by $\pi/2$ around the z axis transforms this Hamiltonian into the same form as the $\mathcal{H}_+$ block of Equation (1.8), with $m + \Delta_{SO}$ replaced by $m_\pm(k_z)$:

$$\mathcal{H}_\pm = -i\hbar v_F \frac{\partial}{\partial x}\sigma^x + \hbar v_F \left(-i\frac{\partial}{\partial y} + \frac{x}{\ell^2} \right) \sigma^y + m_\pm(k_z)\sigma^z. \tag{3.16}$$
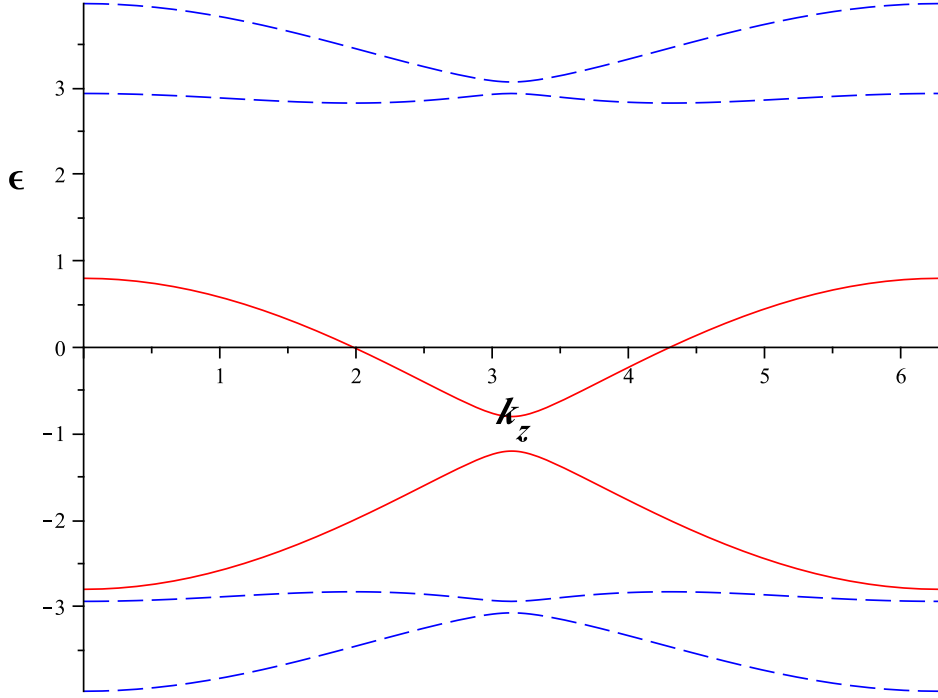
Figure 3.6: Plot of the $N = 0$ (solid lines) and $N = 1$ (dashed lines) Landau levels of the Weyl semimetal, subject to a magnetic field perpendicular to the layers (arbitrary units).

Similarly to Section 1.1.3, then,

$$\mathcal{H}_\pm^2 = 2\hbar^2\omega_B^2(n + \frac{1}{2}) + \hbar^2\omega_B^2 + m_\pm(k_z)^2, \tag{3.17}$$

where $\omega_B = v_F/\ell$. Following the reasoning of Section 1.1.3, the Landau levels are

$$|\epsilon_{N\pm}| = \sqrt{2\hbar^2\omega_B^2 N + [b \pm \Delta(k_z)]^2}. \tag{3.18}$$

As in Section 1.1.3, there are pairs of Landau levels symmetric about $\epsilon = 0$ for $N \geq 1$, but not for $N = 0$. The $N = 0$ levels are $\epsilon_{0+} = -b - \Delta(k_z)$, which is always negative, and $\epsilon_{0-} = -b + \Delta(k_z)$, which changes sign at the Weyl nodes, as shown in Figure 3.6, resulting in an extra filled Landau level and a Hall conductance e^2/h for $|\pi/d - k_z| < k_0$.

Since these lowest Landau levels only depend on the field through b (and not ω_B), which can be generated either by an external field or ferromagnetic impurities, this result for the Hall conductance applies equally to the case of ferromagnetic impurities without an

33

external field, as in Section 3.1, even though the Landau levels do not exist when $B = 0$. The external field case described here may be more easily implemented experimentally, but it is perhaps more interesting from a theoretical point of view to generate a non-zero Hall conductivity without any external field.

Chapter 4

Line Node Semimetal

Another topological semimetal phase, distinct from the Weyl semimetal, is created by applying a TR-breaking field similar to the one that creates the Weyl semimetal, but in a different direction. A term $b\sigma^x$ can be generated by ferromagnetic impurities with their magnetic moments aligned along the planes of the layers forming the system. Added to the Hamiltonian (2.35), this term yields

$$\mathcal{H}(\mathbf{k}) = \hbar v_F \tau^z \left(\hat{z} \times \boldsymbol{\sigma} \right) \cdot \mathbf{k} + \hat{\Delta}(k_z) + b\sigma^x. \tag{4.1}$$

Diagonalizing this Hamiltonian gives the band structure

$$|\epsilon_\pm| = \sqrt{\hbar^2 v_F^2 k_x^2 + \left[b \pm \sqrt{\hbar^2 v_F^2 k_y^2 + \Delta(k_z)^2} \right]^2}, \tag{4.2}$$

shown in Figure 4.1. For $b > |\Delta_S - \Delta_D|$, ϵ_- vanishes along a curve in the y-z plane defined by $\hbar^2 v_F^2 + \Delta(k_z)^2 = b^2$. The state is therefore termed a line node semimetal.

This state is a three-dimensional generalization of the system discussed in Section 2.1; the two-dimensional Hamiltonian obtained by fixing a particular value of k_z in Equation (4.1) is Equation (2.9), with $\Delta_S = \Delta(k_z)$. Thus, many of the results from that section also apply to the line node semimetal. Along any surface not parallel to the x axis, there are gapless surface states, meaning that the surface energy bands meet in the entire region enclosed by the line node, as shown in Figure 4.2. Heikikilä et al showed in [11, 15] that such a flat band leads to a finite specific heat at low temperatures and superconducting behaviour. Section 4.1 will discuss these surface states in more detail, with a focus on symmetry and stability considerations that were not discussed in Section 2.1. There is also a clear transition in the magnetic susceptibility, as in Section 2.1.4, but in this case
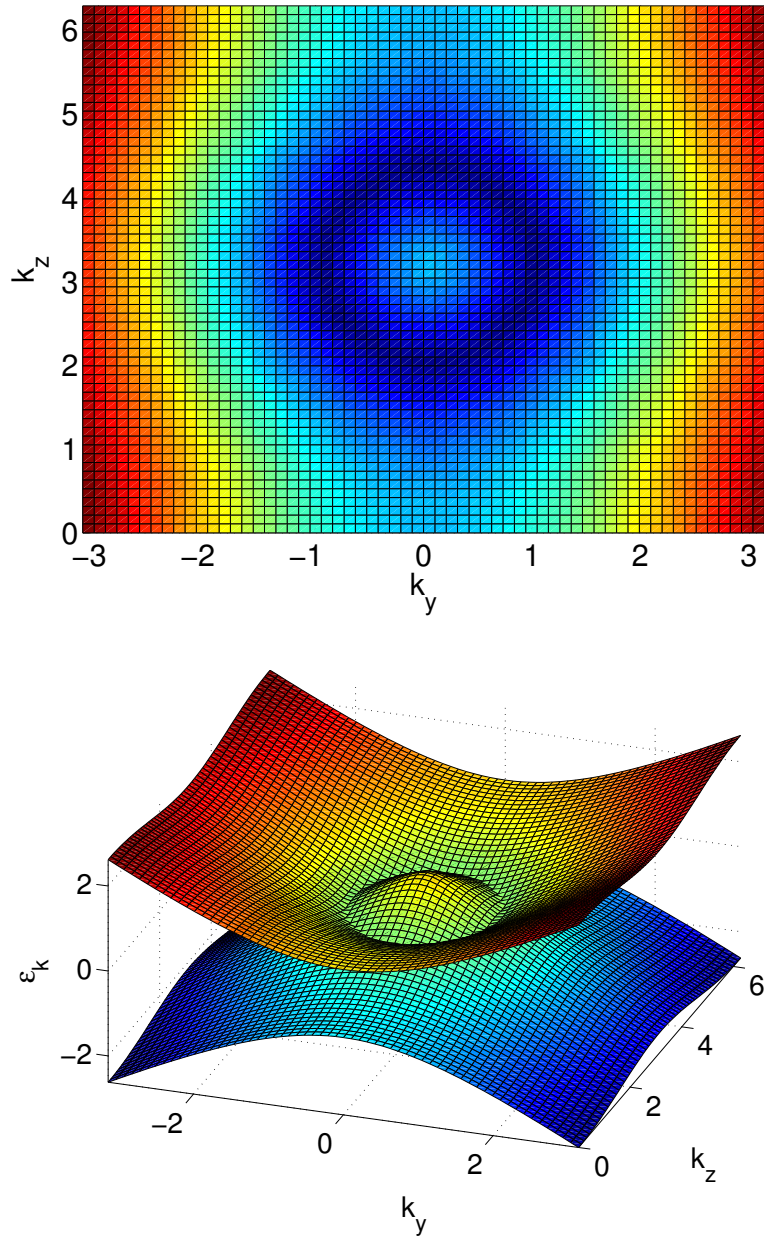
Figure 4.1: Electronic band structure of the line node semimetal plotted as a function of (dimensionless) k_y and k_z for $\Delta_S = 1, \Delta_D = 0.8$, and $k_x = 0$, showing a nearly circular curve of zero-energy states.
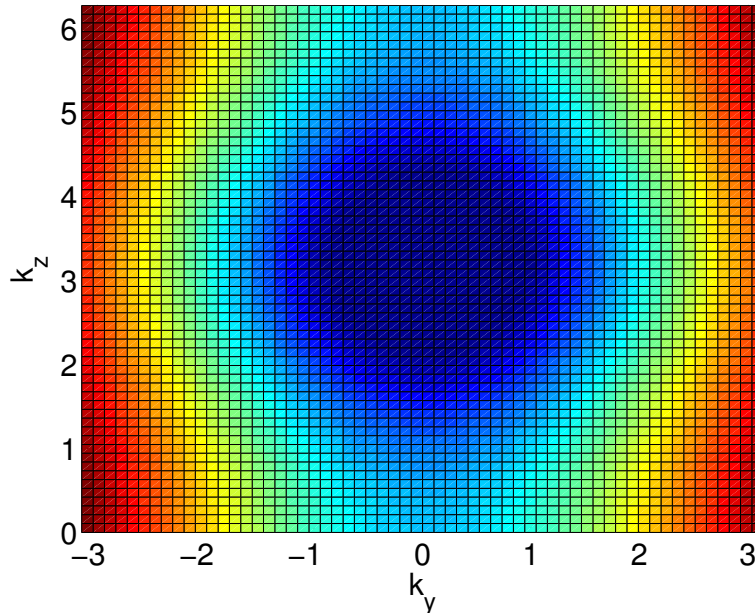
Figure 4.2: Electronic band structure for a sample of the line node semimetal that is finite along the x-axis, showing zero-energy surface states as a dark region in the area enclosed by the line node of Figure 4.1 ($\Delta_S = 1$ and $\Delta_D = 0.8$ as in Figure 4.1).

the susceptibility vanishes not at the onset of the nodal phase, but when the TR-breaking is strong enough that the line node extends across the entire Brillouin zone, as will be explained in Section 4.2.

4.1 Stability of the Nodal Line and Surface States

As in Section 2.1.2, the gapless surface states are guaranteed are guaranteed by the winding of the vector $\mathbf{g} = -\hbar v_F \sin(k_x)\hat{y} + \left[\frac{b}{2}(1 + \cos(k_x)) - b_c\right]\hat{z}$, with $b_c = \sqrt{\hbar^2 v_F^2 k_y^2 + \Delta(k_z)^2}$ in the three-dimensional case. However, this winding is only well-defined when $\mathbf{g}$ has no component in the $\hat{x}$ direction, i.e., the transformed Hamiltonian (2.14) has no σ^x term. A more intuitive reason for this requirement will now be given, along with an argument from symmetry suggesting that this assumption is physically justified in the two-dimensional case and in a particular subset of the Brillouin zone for the three-dimensional case.

Together with the identity operator, the Pauli operators σ^x, σ^y, and σ^z form a basis for the set of Hermitian operators acting on a two-dimensional Hilbert space. Any two-band Hamiltonian can therefore be written as

$$\mathcal{H}(\mathbf{k}) = h_0(\mathbf{k}) + h_1(\mathbf{k})\sigma^x + h_2(\mathbf{k})\sigma^y + h_3(\mathbf{k})\sigma^z. \tag{4.3}$$

The bands touch at a point $\mathbf{k}$ if $h_1(\mathbf{k}) = h_2(\mathbf{k}) = h_3(\mathbf{k}) = 0$. In general, one parameter must be tuned for each component of h that is to vanish; a system of n equations with fewer than n free variables typically does not have a solution. So in order to achieve band-touching, all three components of the momentum must be tuned, giving only discrete band-touching points and not the line node desired in this section. However, if one component of h vanishes everywhere for physical reasons, such as a discrete symmetry of the system, then one free parameter will remain after tuning two momenta, resulting in a continuous line of band-touching points. Similarly, Section 2.1 was concerned with point nodes, but in a two-dimensional system, meaning that only two momentum components were available as tuning parameters, so the extra condition $g_x = 0$ was required to ensure band-touching. The band touching, in turn, was required for the change in topology between the topologically trivial phase for $|k_y| > \frac{1}{\hbar v_F}\sqrt{b^2 - \Delta_S^2}$ and the non-trivial phase when $|k_y| < \frac{1}{\hbar v_F}\sqrt{b^2 - \Delta_S^2}$, by the usual argument that a change in topology necessitates a closing of the energy gap.

It will now be shown, following [3], that the nodal line and corresponding surface states actually do follow from symmetries of the system. The transformations that led to the Hamiltonian (2.14) were as follows. First, the spin axis was rotated by $\pi/2$ around the y axis, then the transformations $\sigma^\pm \to \tau^z \sigma^\pm, \tau^\pm \to \sigma^z \tau^\pm$ were applied, and finally the Hamiltonian was projected onto a 2×2 sub-block by replacing the operator $\hbar v_F k_y \tau^z + b + \Delta_S \tau^x$ with its eigenvalue $b - \sqrt{\hbar^2 v_F^2 k_y^2 + \Delta_S^2}$.

In the current three-dimensional case, the transformed Hamiltonian corresponding to (2.13) is

$$\mathcal{H}'(\mathbf{k}) = \left[\hbar v_F k_y \tau^z + b + \Delta_S \tau^x + \frac{1}{2}\Delta_D \left(\tau^+ e^{ik_z d} + \tau^- e^{-ik_z d}\right)\right]\sigma^z - \hbar v_F k_x \sigma^y. \tag{4.4}$$

The operator in square brackets is projected onto its eigenvalues, giving

$$\mathcal{H}'_\pm(\mathbf{k}) = m_\pm(\mathbf{k})\sigma^z - \hbar v_F \sigma^y k_x, \tag{4.5}$$

where $m_\pm(\mathbf{k}) = b \pm \sqrt{\hbar^2 v_F^2 k_y^2 + \Delta(k_z)^2}$.

The goal of this section, therefore, is to find a set of physical symmetries of (4.1) that, after being subjected to the transformations above, imply that $g_x = 0$. A reflection of the system in the y-z plane reverses the x component of the momentum, and, since spin is a pseudovector, flips the y and z components of the spin. This operation is the composition of two of the symmetry operations in [3]. Mathematically, the reflection is described by the operator

$$R_{yz} : \mathcal{H}(k_x, k_y, k_z) \to \sigma^x \mathcal{H}(-k_x, k_y, k_z)\sigma^x. \tag{4.6}$$

It can be easily verified that (4.1) is invariant under this transformation. Applying the above transformations to R_{yz} gives

$$R'_{yz} : \mathcal{H}'_{\pm}(k_x, k_y, k_z) \to \sigma^z \mathcal{H}'_{\pm}(-k_x, k_y, k_z)\sigma^z. \tag{4.7}$$

Requiring 4.3 to be unchanged by this transformation means that $-h_1(-k_x, k_y, k_z) = h_1(k_x, k_y, k_z)$. In particular, then, $-h_1(0, k_y, k_z) = h_1(0, k_y, k_z)$, so that $h_1(\mathbf{k})$ must vanish on the entire y-z plane. This result is not sufficient for the argument in Section 2.1.2, where it was assumed that the σ^x term vanished for all k_x. However, a stronger argument can be made, making use of another discrete symmetry.

First, the stability of the line node must be established. By the same reasoning used for h_1, h_2 is also an odd function of k_x. Therefore, h_1 and h_2 both vanish along the y-z plane, where the generic two-band Hamiltonian (4.3) can thus be written as

$$\mathcal{H}(k_y, k_z) = h_0(k_y, k_z) + h_3(k_y, k_z)\sigma^z. \tag{4.8}$$

There are then two parameters (k_y and k_z) available to tune h_3 to zero, meaning that the bands touch along a line in the y-z plane.

Another symmetry is required to guarantee the existence of the surface states. Though time-reversal symmetry is broken by the magnetic impurities, the TR operator of Section 1.4 can be combined with a rotation by π about the z axis,

$$\mathcal{R}^z_\pi : \mathcal{H}(k_x, k_y, k_z) \to \sigma^z \mathcal{H}(-k_x, -k_y, k_z)\sigma^z. \tag{4.9}$$

This combination gives a new symmetry operation,

$$\mathcal{T} \circ \mathcal{R}^z_\pi : \mathcal{H}(k_x, k_y, k_z) \to \sigma^x \mathcal{H}^*(k_x, k_y, -k_z)\sigma^x, \tag{4.10}$$

under which (4.1) is invariant. Applying the transformations that led to the block diagonal form of the Hamiltonian, the symmetry operation becomes

$$\mathcal{T}' \circ \mathcal{R}^{z\prime}_\pi : \mathcal{H}'_{\pm}(k_x, k_y, k_z) \to \sigma^z [\mathcal{H}'_{\pm}(k_x, k_y, -k_z)]^* \sigma^z. \tag{4.11}$$

Applied to h_1, this new symmetry implies $h_1(k_x, k_y, k_z) = -h_1(k_x, k_y, -k_z)$, so that h_1 is also an odd function of k_z. In particular, $h_1(k_x, k_y, \pi/d) = -h_1(k_x, k_y, -\pi/d)$, which means that $h_1(k_x, k_y, \pi/d) = 0$, since $k_z = \pi/d$ and $k_z = -\pi/d$ define equivalent surfaces in the Brillouin zone. So, fixing $k_z = \pi/d$, the transformed Hamiltonian becomes (2.14), with Δ_S replaced by $\Delta(\pi/d) = \sqrt{\Delta_S^2 + \Delta_D^2 - 2\Delta_S\Delta_D} = |\Delta_S - \Delta_D|$. The argument from Section 2.1.2 then applies, showing that there is a non-trivial winding of $\mathbf{g}$ for $b > |\Delta_S - \Delta_D|$ and k_y between the two points where the nodal line intersects the $k_z = \pi/d$ plane. This winding implies the existence of gapless edge states along the line segment $k_z = \pi/d$, $|k_y| < \frac{1}{\hbar v_F}\sqrt{b^2 - |\Delta_S - \Delta_D|}$. Thus, the gapless edge states of the single-layered system in Section 2.1 are fully protected by symmetry, while in the full three-dimensional system, only the line $k_z = \pi/d$ is protected.

To demonstrate this partial protection by symmetry, one can consider perturbing the Hamiltonian (4.1) by the addition of a term that respects the above symmetries. For instance, the term $\mathcal{H}_p(\mathbf{k}) = ak_xk_y\sin(k_zd)\sigma^z\tau^z$ is invariant under the symmetry operations above, as well as the inversion and the rotation by π around the x axis described in [3]. Since $\mathcal{H}_p(\mathbf{k}) = 0$ when $k_x = 0$, the bulk nodal line is unaffected by this perturbation. However, applying the same rotation, transformation, and projection that gave (4.5), $\mathcal{H}_p(\mathbf{k})$ becomes $\mathcal{H}'_p(\mathbf{k}) = -ak_xk_y\sin(k_zd)\sigma^x$, showing that the above symmetries are not sufficient to prevent a σ^x term from arising in some regions of momentum space. Calculating the electron energies for a system with a surface perpendicular to the x axis shows that the gapless surface states are eliminated, except along the lines $k_y = 0$ (which is enforced by the inversion and rotation symmetries of [3]) and $k_z = \pi/d$, as argued above. The results of this calculation are plotted in Figure 4.3.

The symmetries of the Hamiltonian (4.1) also do not protect against an h_0 term in Equation (4.3). This term shifts the energy of a state with momentum $\mathbf{k}$ by $h_0(\mathbf{k})$, which does not eliminate either the band-touching or the surface states, but since $h_0(\mathbf{k})$ need not be constant, it will generally shift the line node non-uniformly in energy, giving the system a Fermi surface with finite volume as described in [3].

4.2   Magnetic Susceptibility

The susceptibility of the line node semimetal is quite similar to that of the single-layered system with applied magnetic field, and can be calculated in nearly the same way. In this case, the orbital part of the magnetic field is neglected for simplicity, so that $b = g\mu_B B/2$.
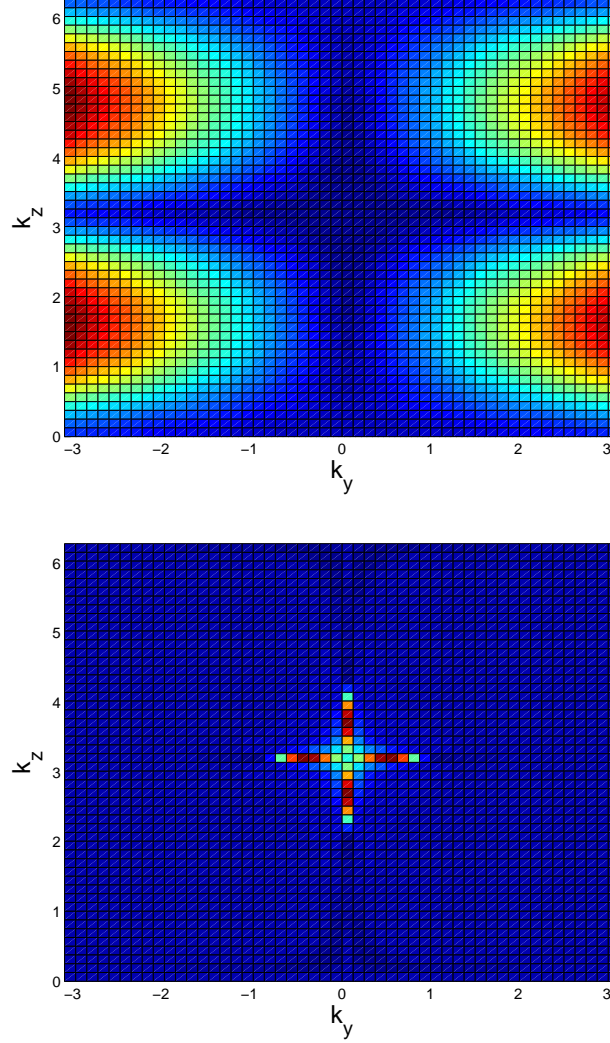
Figure 4.3: Top: Band structure of the line node semimetal for a sample that is finite in the x direction, subject to the symmetry-preserving perturbation $\mathcal{H}_p(\mathbf{k})$ described in the text. The zero-energy states are eliminated except along the lines $k_y = 0$ and $k_z = \pi$. Bottom: Plot of the inverse participation ratio (defined in Section 2.1.3) corresponding to the energy states of the upper plot, providing an indication of the extent to which electron wavefunctions are localized to the surface of the material. The dark region corresponds to bulk states, while the coloured lines along $k_y = 0$ and $k_z = \pi$ are the surviving gapless surface states.

41

Once again, the free energy is

$$F = -k_B T \sum_{\mathbf{k}} \left[\ln\left(1 + e^{-\frac{\epsilon_{\mathbf{k},+} - \mu}{k_B T}}\right) + \ln\left(1 + e^{-\frac{\epsilon_{\mathbf{k},-} - \mu}{k_B T}}\right) \right.$$
$$\left. + \ln\left(1 + e^{\frac{\epsilon_{\mathbf{k},+} + \mu}{k_B T}}\right) + \ln\left(1 + e^{\frac{\epsilon_{\mathbf{k},-} + \mu}{k_B T}}\right) \right], \tag{4.12}$$

with the band dispersion $\epsilon_{\mathbf{k},\pm}$ now given by Equation (4.2). The susceptibility in this case is

$$\chi(B) = -\frac{1}{V}\frac{\partial^2 F}{\partial B^2}, \tag{4.13}$$

where V is the volume of the sample. The same calculation as in Section 2.1.4 gives

$$\chi(B) = V\left(\frac{\mathrm{d}b}{\mathrm{d}B}\right)^2 \mathcal{I}(B), \tag{4.14}$$

where

$$\mathcal{I}(B) = \int \frac{\mathrm{d}^3 k}{8\pi^3}\, \hbar^2 v_F^2 k_x^2 \left[\frac{1}{\epsilon_{\mathbf{k},+}^3} + \frac{1}{\epsilon_{\mathbf{k},-}^3} - \frac{1}{\epsilon_{\mathbf{k},+}^3}\bigg|_{\Delta(k_z)=0} - \frac{1}{\epsilon_{\mathbf{k},-}^3}\bigg|_{\Delta(k_z)=0} \right]. \tag{4.15}$$

Integrating over k_x and k_y leads to

$$\mathcal{I}(B) = \int \mathrm{d}k_z\, \mathcal{I}_{k_z}(B), \tag{4.16}$$

where

$$\mathcal{I}_{k_z}(B) = \begin{cases} -\frac{1}{2\pi^2 v_F^2}\sqrt{\Delta(k_z)^2 - b^2} & \text{if } \Delta(k_z)^2 - b^2 \geq 0 \\ 0 & \text{if } \Delta(k_z)^2 - b^2 < 0. \end{cases} \tag{4.17}$$

$\chi(B)$ can then be computed numerically to give the result shown in Figure 4.4. One can see from Equation (4.17) that $\chi(B) = 0$ if $\Delta(k_z)^2 < b^2$ for all k_z or, equivalently, if $b > \Delta_S + \Delta_D$. This condition is stronger than the one for the formation of the nodal line, $b > |\Delta_S - \Delta_D|$, and corresponds to a special situation in which the nodal line extends across the entire length of the Brillouin zone, as shown in Figure 4.5.

This result can be readily interpreted in relation to the two-dimensional system of Section 2.1. As mentioned previously, the line node semimetal, at fixed k_z, reduces to a two-dimensional system that is identical to the single layer system discussed in Section 2.1. Depending on the values of k_z, b, Δ_S, and Δ_D, the reduced system may be in either

42

an insulating or a semimetallic phase. If a plane of fixed k_z intersects the nodal line, the two-dimensional reduced system has point nodes at these intersection points and is therefore semimetallic with zero susceptibility, as calculated in Section 2.1.4. But if the plane does not intersect the nodal line, the reduced system is fully gapped and therefore insulating, with the diamagnetic response of Section 2.1.4. When $b < \Delta_S + \Delta_D$, both situations occur for some values of k_z, and the insulating sections contribute to a non-zero diamagnetic response. When $b > \Delta_S + \Delta_D$, however, the nodal line extends across the entire Brillouin zone, so it intersects all fixed-k_z planes. meaning that all the reduced systems are semimetallic and the total susceptibility is zero.

Near the transition to this state, when b is slightly smaller than $\Delta_S + \Delta_D$, $\chi(B)$ can be calculated analytically by approximating $\Delta(k_z)$ near $k_z = 0$, where the non-zero contribution to $\mathcal{I}(B)$ occurs. In this case, $\Delta(k_z)^2 \approx (\Delta_S + \Delta_D)^2 - \Delta_S \Delta_D k_z^2$. So

$$\mathcal{I}(B) \approx -\frac{1}{2\pi^2 v_F^2} \int \mathrm{d}k_z \left[\sqrt{(\Delta_S + \Delta_D)^2 - b^2 - \Delta_S \Delta_D k_z^2} \right], \tag{4.18}$$

with the integral taken over all values of k_z for which the argument of the square root is non-negative. Evaluating the integral gives the final result for the susceptibility

$$\chi(B) \approx -\left(\frac{g\hbar e}{4mc} \right)^2 \frac{(\Delta_S + \Delta_D)^2 - b^2}{4\pi v_F^2 \sqrt{\Delta_S \Delta_D}}, \tag{4.19}$$

when $\frac{(\Delta_S + \Delta_D)^2 - b^2}{\Delta_S \Delta_D}$ is small, i.e., when $\Delta(0)$ and b are similar in magnitude, so that only values of k_z close to zero contribute to the integral.

4.3 Effect of Orbital Field

As mentioned in Chapter 3, it may be experimentally simpler to break time-reversal symmetry by applying an external magnetic field to a (relatively) pure sample rather than by doping the layered structure with ferromagnetically-aligning impurities. However, an in-plane external field (corresponding to the in-plane ferromagnetic alignment that led to the line node) adds considerable mathematical complexity to the description of the system. Again using the Landau gauge, the vector potential corresponding to a field $\mathbf{B} = B\hat{x}$ is $\mathbf{A} = -zB\hat{y}$. Making the substitution $\mathbf{k} \to -i\nabla + \frac{e}{\hbar c}\mathbf{A}$ in the model Hamiltonian (2.2) gives

$$\mathcal{H} = \hbar v_F \tau^z (\hat{z} \times \boldsymbol{\sigma}) \cdot \left(-i\nabla - \frac{eBz}{\hbar c}\hat{y} \right) + \frac{g\mu_B}{2}B\sigma^x + \hat{\Delta}, \tag{4.20}$$

43
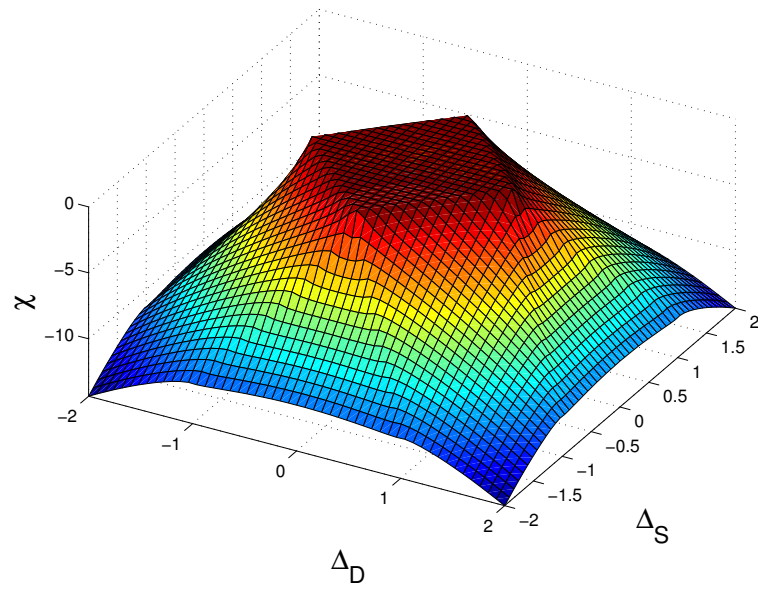
Figure 4.4: Susceptibility of the line node semimetal for $b = 1$, showing zero susceptibility when $b \geq \Delta_S + \Delta_D$, corresponding to Figure 4.5 (c) and (d).
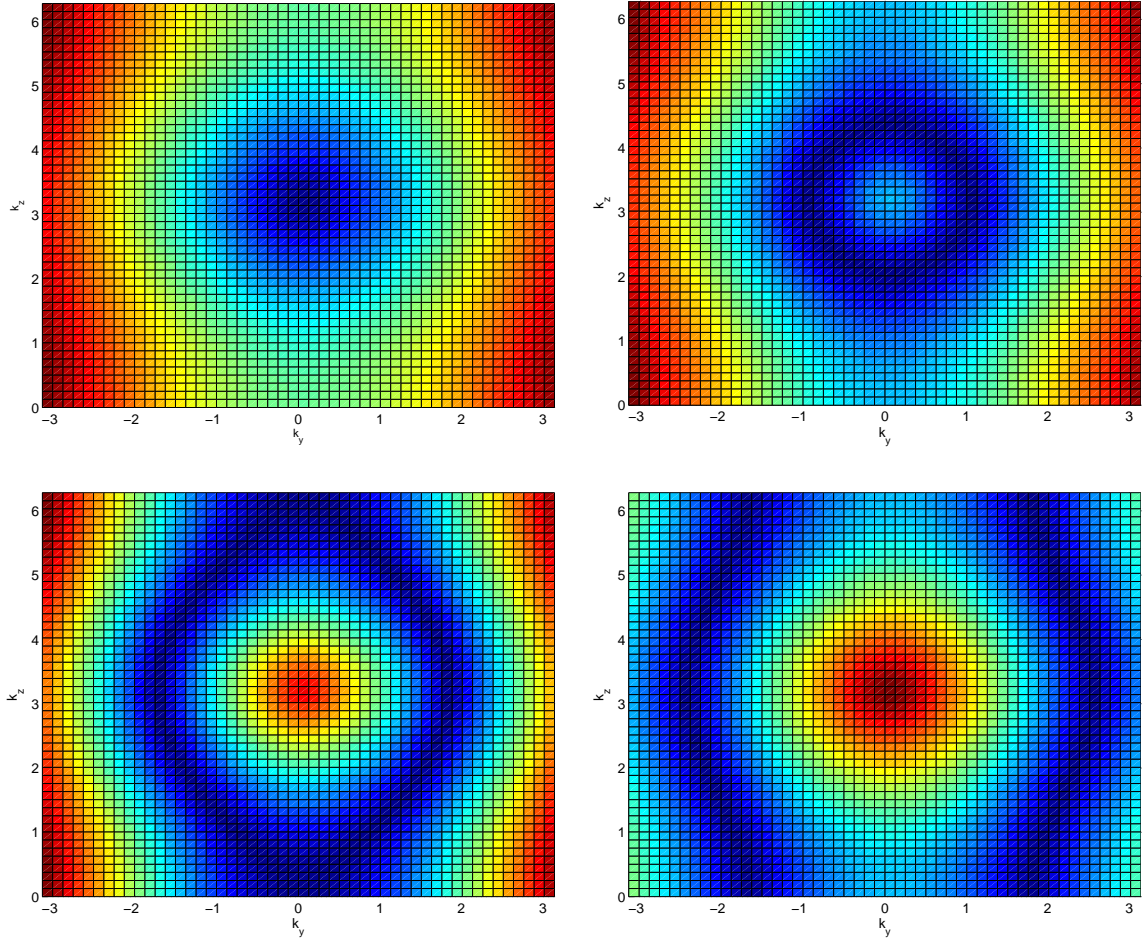
Figure 4.5: Representative plots of the band structure of the line node semimetal, showing different shapes of the line node (dark lines): (a) $b = |\Delta_S - \Delta_D|$: the node is a single point; (b) $|\Delta_S - \Delta_D| < b < \Delta_S + \Delta_D$: the node is a closed curve contained entirely within the Brillouin zone; (c) $b = \Delta_S + \Delta_D$: the line node just touches the edges of the Brillouin zone at $k_z = 0$ and $k_z = 2\pi/d$; (d) $b > \Delta_S + \Delta_D$: there are two separate line nodes, each crossing the entire Brillouin zone.

where $\hat{\Delta}$ is the tunneling operator $\Delta_S \tau^x \delta_{i,j} + \frac{1}{2}\Delta_D(\tau^+ \delta_{j,i+1} + \tau^- \delta_{j,i-1})$ from Equation (2.2).

Because the vector potential $\mathbf{A}$ is a function of z in this case, $\mathcal{H}$ cannot be brought to a simple 4×4 form by a Fourier transform $c^\dagger_{\mathbf{k}_\perp,j} = \sum_{k_z} c^\dagger_{\mathbf{k}} e^{-ik_z dj}$ as was done in Section 2.2; the problem can only be solved numerically. [3] However, there are two limiting cases for which the behaviour can be studied analytically.

4.3.1 Almost Decoupled TI Layers: $\Delta_D \ll \Delta_S$

The simplest case is that of thin TI layers and thick ordinary insulator layers, meaning that the coupling between opposite surfaces of the same layer is much stronger than that between adjacent layers. In this case, Δ_D is neglected so that $\hat{\Delta} = \Delta_S \tau^x$ and the Hamiltonian can be written as a sum of independent Hamiltonians describing individual layers, similar to Equation (2.6):

$$\mathcal{H}(\mathbf{k}_\perp, j) = \hbar v_F \tau^z (\hat{z} \times \boldsymbol{\sigma}) \cdot \left(\mathbf{k} - \frac{eB}{\hbar c}\left(dj + \frac{d_{\mathrm{TI}}}{2}\tau^z \right) \hat{y} \right) + \frac{g\mu_B B}{2}\sigma^x + \Delta_S \tau^x, \qquad (4.21)$$

where j labels each of the TI layers, d is the period of the layered structure, and d_{TI} is the thickness of a single TI layer. Since different layers do not interact, the dj term can be eliminated by translating the momentum of layer j via $\mathbf{k} \to \mathbf{k} + \frac{eB}{\hbar c}dj\hat{y}$, giving

$$\mathcal{H}(\mathbf{k}) = \hbar v_F \tau^z (\hat{z} \times \boldsymbol{\sigma}) \cdot \left(\mathbf{k} - \frac{eB}{\hbar c}\frac{d_{\mathrm{TI}}}{2}\tau^z \hat{y} \right) + \Delta_S \tau^x + \frac{ge\hbar}{4mc}B\sigma^x, \qquad (4.22)$$

which is precisely Equation (2.6) except that $\mathbf{k}$ is three-dimensional, with $\mathcal{H}(\mathbf{k})$ completely independent of k_z. Thus, the system reduces to multiple copies of the single layer of Section 2.1 and Reference [27], with corresponding properties. As before, defining $b = \left(\frac{g\hbar^2}{4m\ell^2} - \frac{\hbar v_F d_{\mathrm{TI}}}{2\ell^2} \right)$ with $\ell = \sqrt{\frac{\hbar c}{eB}}$, the bands touch, yielding a semimetallic phase when $b > \Delta_S$. This band-touching now occurs along two vertical lines in momentum space defined by $k_x = 0$, $k_y = \pm\sqrt{b^2 - \Delta_S^2}$. Between these two line nodes, there are topological surface states that are dispersionless in the $\hat{y}$ direction by the same argument as in Section 2.1.2, and trivially dispersionless in the $\hat{z}$ direction. These surface states are simply the edge states from Section 2.1.2, occurring on each TI layer.

4.3.2 Weak Field

A more interesting limit is that of $\frac{g\mu_B B}{2} \ll \Delta_S + \Delta_D$ and $|\Delta_S - \Delta_D| \ll \Delta_S + \Delta_D$, corresponding to a weak magnetic field and nearly equal tunneling amplitudes. The line node

46

is expected to be small in this case, so that $\hat{\Delta}(k_z)$ can be expanded near π/d, giving $\hat{\Delta}(k_z) \approx (\Delta_S - \Delta_D)\tau^x + \Delta_D k_z d\tau^y$. In a full real-space description, the Hamiltonian is then

$$\mathcal{H} = \hbar v_F \tau^z (\hat{z} \times \boldsymbol{\sigma}) \cdot \left(-i\nabla - \frac{eBz}{\hbar c}\hat{y} \right) + \frac{g\mu_B B}{2}\sigma^x + (\Delta_S - \Delta_D)\tau^x - i\Delta_D \tau^y \frac{\partial}{\partial z}. \quad (4.23)$$

After the rotation of the spin axis by $\pi/2$ around the y axis and transforming $\sigma^\pm \to \tau^z \sigma^\pm$, $\tau^\pm \to \sigma^z \tau^\pm$, as in (2.12), the Hamiltonian is

$$\mathcal{H}' = [b + \hbar v_F \tau^z \pi_y + \Delta_D d\tau^y \pi_z + (\Delta_S - \Delta_D)\tau^x]\sigma^z - \hbar v_F k_x \sigma^y, \quad (4.24)$$

where $\boldsymbol{\pi} = -i\frac{\partial}{\partial x}\hat{x} + \left(-i\frac{\partial}{\partial y} - \frac{z}{\ell^2} \right)\hat{y} - i\frac{\partial}{\partial z}\hat{z}$ is the kinetic momentum, $\ell = \sqrt{\frac{\hbar c}{eB}}$ is the magnetic length, and k_x has been restored because the Hamiltonian is independent of x. The τ operator terms will be studied first: the operator $\mathcal{H}_L = \hbar v_F \tau^z \pi_y + \Delta_D d\tau^y \pi_z + (\Delta_S - \Delta_D)\tau^x$ is similar to the Hamiltonian of Equation (1.8) and has a corresponding spectrum of Landau levels. $\mathcal{H}_L$ commutes with $\mathcal{H}'$, so it can be diagonalized separately. In this case, the Landau energies are calculated by introducing ladder operators:

$$\pi_y = \sqrt{\frac{\tilde{v}_F}{2v_F \ell^2}}(a^\dagger + a),$$
$$\pi_z = -i\sqrt{\frac{v_F}{2\tilde{v}_F \ell^2}}(a^\dagger - a), \quad (4.25)$$

where $\tilde{v}_F = \frac{d}{\hbar}\sqrt{\Delta_S \Delta_D} \approx \frac{d\Delta_D}{\hbar}$. These can be shown from the definitions of π_y and π_z to have the commutator $[a, a^\dagger] = 1$, as required for ladder operators. Dropping the $\Delta_S - \Delta_D$ term and inserting (4.25), $\mathcal{H}_L$ becomes

$$\mathcal{H}_L = \frac{\hbar\omega_B}{\sqrt{2}}\left[\tau^z(a^\dagger + a) - i\tau^y(a^\dagger - a) \right], \quad (4.26)$$

where $\omega_B = \sqrt{v_F \tilde{v}_F}$. Acting on $|n\rangle$, the nth eigenstate of the number operator $a^\dagger a$, $\mathcal{H}_L$ gives

$$\mathcal{H}_L|n\rangle = \frac{\hbar\omega_B}{\sqrt{2}}\left[\tau^z\left(\sqrt{n+1}\,|n+1\rangle + \sqrt{n}\,|n-1\rangle \right) - i\tau^y\left(\sqrt{n+1}\,|n+1\rangle + \sqrt{n}\,|n-1\rangle \right) \right], \quad (4.27)$$

which has eigenvalues

$$\epsilon_{n\pm} = \pm\sqrt{2\hbar^2\omega_B^2 n}. \quad (4.28)$$

47

The full Hamiltonian therefore becomes

$$\mathcal{H}_n(k_x) = \left[b \pm \sqrt{2\hbar^2\omega_B^2 n} \right] \sigma^z - \hbar v_F k_x \sigma^y. \tag{4.29}$$

This is the same as the Hamiltonian (2.14) with b_c replaced by $\sqrt{2\hbar^2\omega_B^2 n}$, so the same topological argument used in Section 2.1.2 implies that there are zero-energy surface states when $b > \sqrt{2\hbar^2\omega_B^2 n}$.

Chapter 5

Transport Properties of Semimetallic Phases

This chapter focuses on the interesting transport properties of the semimetallic phases. The results apply to Weyl fermions or line node semimetals with the same band structure in general and are not specific to the particular model discussed previously.

5.1 Point Impurities

The simplest case studied here is that of non-interacting electrons, scattered only by short-range potentials around impurities in the material:

$$V(\mathbf{r}) = u_0 \sum_a \delta(\mathbf{r} - \mathbf{r}_a), \tag{5.1}$$

where $\mathbf{r}_a$ labels the position of impurity a. This is an overly simplistic model, but it is accurate when the temperature is high and the Fermi energy is close to the Weyl nodes.

Only electrons close to the Fermi energy (assumed here to be $\epsilon_F = 0$) contribute to the conductivity, so the band dispersion

$$\epsilon_k = \sqrt{\hbar^2 v_F^2 \left(k_x^2 + k_y^2\right) + \left[b - \Delta(k_z)\right]^2} \tag{5.2}$$

can be approximated near the Weyl nodes as in Equation 3.5, giving

$$\epsilon_k = \sqrt{\hbar^2 v_F^2 (k_x^2 + k_y^2) + \hbar^2 v_z^2 k_z^2}, \tag{5.3}$$

where $v_z = \frac{\Delta_S \Delta_D d \sin(k_0 d)}{b\hbar}$. In order to calculate the conductivity, the corresponding density of states, $g(\epsilon)$, is required. This quantity is calculated by first computing $N(\epsilon)$, the number of electronic states with energies less than or equal to ϵ. The dispersion in (5.3) defines a family of ellipsoidal surfaces of constant energy:

$$\frac{1}{\epsilon^2}\left[\hbar^2 v_F^2 (k_x^2 + k_y^2) + \hbar^2 v_z^2 k_z^2\right] = 1. \tag{5.4}$$

The volume of such an ellipsoid is $\frac{4}{3}\pi \frac{1}{\hbar^3 v_F^2 v_z} \epsilon^3$, so

$$N(\epsilon) = \frac{V}{(2\pi)^3}\frac{4}{3}\pi \frac{1}{\hbar^3 v_F^2 v_z}\epsilon^3. \tag{5.5}$$

Finally,

$$g(\epsilon) = \frac{1}{V}\frac{\mathrm{d}N}{\mathrm{d}\epsilon}$$

$$= \frac{\epsilon^2}{2\pi^2 \hbar^3 v_F^2 v_z} \tag{5.6}$$

The AC conductivity is calculated using the Boltzmann equation:

$$\frac{\partial f}{\partial t} = -\nabla f \cdot \mathbf{v} + \frac{e}{\hbar}(\nabla_{\mathbf{k}} f)\cdot \mathbf{E} - \frac{f - f_0}{\tau}, \tag{5.7}$$

where

$$\tau = \frac{1}{2\pi\hbar\gamma g(\epsilon)} \tag{5.8}$$

is the relaxation time, $\gamma = u_0^2 n_i / \hbar^2$ is a constant, proportional to the density of impurities, n_i, characterizing the ability of impurities to scatter electrons, $f(\mathbf{r}, \mathbf{k}, t)$ is the electron distribution function (the probability density function at time t for finding an electron at position $\mathbf{r}$ with wave number $\mathbf{k}$), and f_0 is the equilibrium distribution function with no applied electric field. The electric field is taken to be $\mathbf{E} = E_0 e^{i\omega t}\hat{x}$. Assuming that the distribution function is spatially uniform means $\nabla f = 0$ in Equation (5.7). It is also assumed that f has the form $f_0 + f_1$, with f_1 proportional to E_0, and terms of order E_0^2 are neglected. Finally, assuming a solution of the form $f_1(t) = f_1 e^{i\omega t}$, Equation (5.7) then takes the form

$$i\omega f_1 = \frac{e}{\hbar}(\nabla_{\mathbf{k}} f_0)\cdot(E_0\hat{x}) - 2\pi\hbar\gamma f_1 g(\epsilon). \tag{5.9}$$

Now $\nabla_{\mathbf{k}} f_0 = \frac{\partial f_0}{\partial \epsilon} \nabla_{\mathbf{k}} \epsilon$, and $\nabla_{\mathbf{k}} \epsilon = \hbar \mathbf{v_k}$, so the final result for f_1 is

$$f_1 = \frac{e \frac{\partial f_0}{\partial \epsilon} \mathbf{v_k} \cdot (E_0 \hat{x})}{i\omega + 2\pi \hbar \gamma g(\epsilon)}. \tag{5.10}$$

There is no current in equilibrium with zero applied field, so f_0 does not contribute to the current, which is then given by

$$\mathbf{j} = -2e^2 e^{i\omega t} \int \frac{\mathrm{d}^3 k}{(2\pi)^3} f_1 \mathbf{v_k}, \tag{5.11}$$

where the factor 2 accounts for the presence of two distinct Weyl nodes. Evaluating $\mathbf{v_k} = \nabla_{\mathbf{k}} \epsilon_{\mathbf{k}}$ explicitly,

$$\mathbf{v_k} = \frac{\hbar v_F^2 (k_x \hat{x} + k_y \hat{y}) + \hbar v_z^2 k_z \hat{z}}{\epsilon_k}. \tag{5.12}$$

At a temperature T, f_0 is the Fermi-Dirac distribution

$$f_0 = \frac{1}{1 + e^{\epsilon_k / k_B T}}, \tag{5.13}$$

so

$$\frac{\partial f_0}{\partial \epsilon} = -\frac{e^{\epsilon_k / k_B T}}{k_B T (1 + e^{\epsilon / k_B T})^2}. \tag{5.14}$$

Combining Equations (5.10), (5.11), (5.12), and (5.14), the in-plane conductivity, σ_{xx}, is then

$$\sigma_{xx} = \frac{2\hbar^2 v_F^4 e^2}{k_B T} \int \frac{\mathrm{d}^3 k}{(2\pi)^3} \frac{e^{\epsilon_k / k_B T}}{\epsilon_k^2 (1 + e^{\epsilon_k / k_B T})^2} \frac{k_x^2}{i\omega + 2\pi \hbar \gamma g(\epsilon_k)}. \tag{5.15}$$

After a simple change of variables $(k_x \to k_x / \hbar v_F,\ k_y \to k_y / \hbar v_F,\ k_z \to k_z / \hbar v_z)$ and switching to spherical coordinates, with $r = \sqrt{k_x^2 + k_y^2 + k_z^2}$ and θ the polar angle from the k_x axis:

$$\sigma_{xx} = \frac{2e^2}{(2\pi)^2 \hbar^3 v_z k_B T} \int_0^\infty \mathrm{d}r\, \frac{e^{r/k_B T}}{(1 + e^{r/k_B T})^2} \frac{r^2}{i\omega + \frac{\gamma}{\pi \hbar^2 v_F^2 v_z} r^2} \int_0^\pi \mathrm{d}\theta\, \cos^2(\theta) \sin(\theta). \tag{5.16}$$

Making another change of variables $(r \to k_B T r)$ and evaluating the integral over θ gives

$$\sigma_{xx} = \frac{e^2 v_F^2}{3\pi \gamma \hbar} \int_0^\infty \mathrm{d}r\, \frac{e^r}{(1 + e^r)^2} \frac{r^2}{i \frac{\pi \hbar^2 v_F^2 v_z}{(k_B T)^2 \gamma} \omega + r^2}. \tag{5.17}$$

51

This can be rewritten in a dimensionless form as

$$\frac{\sigma_{xx}}{\sigma_{DC}} = \int_0^\infty dx \; \text{sech}^2(x) \frac{x^2}{x^2 + i\tilde{\omega}}, \tag{5.18}$$

where $\tilde{\omega} = \frac{\pi \hbar^2 v_F^2 v_z}{4\gamma(k_B T)^2}\omega$ is a dimensionless frequency and

$$\sigma_{DC} = \frac{e^2 v_F^2}{3\gamma h} \tag{5.19}$$

is the conductivity at zero frequency. The real part of Equation (5.18) is

$$\text{Re}(\sigma_{xx}) = \sigma_{DC} \int_0^\infty dx \; \text{sech}^2(x) \frac{x^4}{x^4 + \tilde{\omega}^2}. \tag{5.20}$$

Figure 5.1 shows $\text{Re}(\sigma_{xx})$ plotted as a function of $\tilde{\omega}$. Equation (5.17) shows that, considered as a function of ω, the width of the peak in the conductivity is proportional to T^2. Thus, the width approaches zero for $T \to 0$. This unusual behaviour may be used as evidence to experimentally establish that a particular material is indeed a Weyl semimetal. Figure 5.1 shows non-analytic behaviour at low frequency, which can be studied in more detail. Differentiating Equation (5.20) gives

$$\frac{d\sigma_{xx}}{d\tilde{\omega}} = -2\sigma_{DC}\tilde{\omega} \int_0^\infty dx \; \text{sech}^2(x) \frac{x^4}{(x^4 + \tilde{\omega}^2)^2}. \tag{5.21}$$

The integrand diverges as $\tilde{\omega}$ and x approach zero, so the low-frequency behaviour can be extracted by approximating the integrand near $x = 0$, where the dominant contribution occurs. Thus, taking $\text{sech}^2(x) \approx 1$, the result is

$$\frac{d\sigma_{xx}}{d\tilde{\omega}} = -\frac{\pi\sqrt{2}\sigma_{DC}}{8\sqrt{\tilde{\omega}}}. \tag{5.22}$$

Integrating over $\tilde{\omega}$ to reattain σ_{xx} and restoring the dimensional factors, the conductivity near $\omega = 0$ is

$$\text{Re}(\sigma_{xx}) \approx \frac{e^2 v_F^2}{3\gamma h}\left(1 - \sqrt{\frac{\omega\pi v_F^2 v_z h^2}{16\gamma(k_B T)^2}}\right). \tag{5.23}$$

The behaviour of an ordinary metal, also shown in Figure 5.1 is quite different, having the form

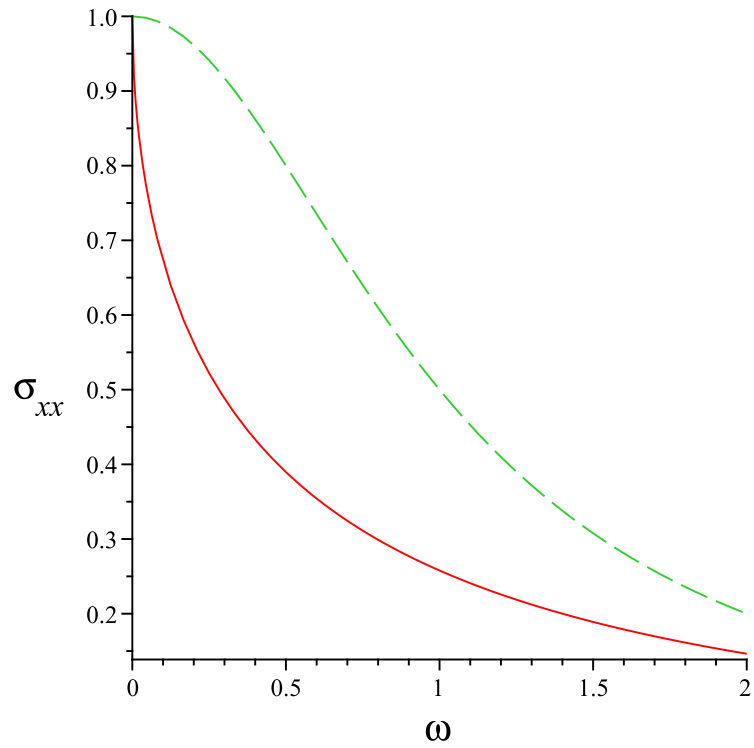$$\sigma = \frac{\sigma_{DC}}{1 + \omega^2\tau^2}. \tag{5.24}$$

Figure 5.1:   Real part of the AC conductivity, $\sigma_{xx}/\sigma_{\mathrm{DC}}$, at finite temperature, plotted as a function of the dimensionless frequency for a Weyl semimetal (solid line) and for an ordinary metal (dashed line).

This behaviour is qualitatively different from that of the Weyl semimetal, with the relaxation time of an ordinary metal being approximately constant at low temperatures, so that the so-called Drude peak of the conductivity has a temperature-independent width and behaves analytically at all frequencies, while, as shown above, the conductivity peak of the Weyl semimetal has a width proportional to T^2 and non-analytic behaviour at $\omega = 0$.

5.2   Donor Impurities

A more realistic model for calculating the conductivity considers donor impurities: electrons escape from these impurities and travel throughout the material, giving a non-zero Fermi energy and leaving behind positively charged impurity ions. In this case, the relaxation time of Equation (5.8) must be replaced by the transport time: [3]

$$\frac{1}{\tau_{\text{tr}}(\epsilon)} = \frac{\pi n_i g(\epsilon)}{\hbar} \int_0^\pi d\theta \ \sin(\theta)|V(q)|^2[1 - \cos(\theta)]\frac{1 + \cos(\theta)}{2}, \tag{5.25}$$

where n_i is the concentration of impurity ions, θ is the scattering angle, $q = w(\epsilon/\hbar v_F)\sin(\theta/2)$, $V(q)$ is the screened Coulomb potential in the Thomas-Fermi approximation,

$$V(q) = \frac{4\pi e^2}{\epsilon_d(q^2 + q_{\text{TF}}^2)}, \tag{5.26}$$

with the Thomas-Fermi wavevector $q_{\text{TF}}^2 = 4\pi e^2 g(\epsilon)$. An effective fine structure constant is defined by $\alpha = e^2/\epsilon_d \hbar v_F$, with ϵ_d the dielectric constant of the material, and can be thought of as the ratio of the Coulomb energy scale $e^2 k_F/\epsilon_d$ to the kinetic energy scale $\hbar v_F k_F$. For this section, the Weyl fermions are assumed to be isotropic, so that $v_z = v_F$. Equation (5.25) then becomes

$$\frac{1}{\tau_{\text{tr}}(\epsilon)} = \frac{\pi \hbar^2 \alpha^2 n_i v_F^3}{4\epsilon^2} \int_0^\pi d\theta \ \frac{\sin^3(\theta)}{\left[\sin^2(\frac{\theta}{2}) + \frac{\alpha}{2\pi}\right]^2}. \tag{5.27}$$

Evaluating the integral gives

$$\frac{1}{\tau_{\text{tr}}(\epsilon)} = \frac{4\pi^3 \hbar^2 n_i v_F^4}{3\epsilon^2} f(\alpha), \tag{5.28}$$

where

$$f(\alpha) = \frac{3\alpha^2}{\pi^2} \left[(1 + \alpha/\pi)\tanh^{-1}\left(\frac{1}{1 + \alpha/\pi}\right) - 1\right]. \tag{5.29}$$

54

When the Coulomb energy is much larger than the kinetic energy, $\alpha \gg 1$ and $f(\alpha) \approx 1$, while for weak Coulomb interactions, $\alpha \ll 1$ and

$$f(\alpha) \approx \frac{3\alpha^2}{2\pi^3} \ln\left(\frac{1}{\alpha}\right). \tag{5.30}$$

Following the Boltzmann equation method of Section 5.1 and focusing on the DC conductivity at zero temperature, the equation corresponding to (5.10) using the transport time (5.28) is

$$f_1 = eE\tau_{\text{tr}}(\epsilon)\frac{\partial f_0}{\partial \epsilon}\mathbf{v_k} \cdot \hat{x}. \tag{5.31}$$

At zero temperature, $\frac{\partial f_0}{\partial \epsilon} = -\delta(\epsilon - \epsilon_F)$, so the in-plane DC conductivity is

$$\sigma_{xx} = 2e^2 \int \frac{d^3k}{(2\pi)^3}\tau_{\text{tr}}(\epsilon_\mathbf{k})\delta(\epsilon_\mathbf{k} - \epsilon_F)\frac{\hbar^2 v_F^4 k_x^2}{\epsilon_\mathbf{k}^2}. \tag{5.32}$$

Inserting $g(\epsilon_\mathbf{k})$ from (5.6) and changing to spherical coordinates:

$$\sigma_{\text{DC}} = \frac{\hbar^5 v_F^7 e^2}{2\pi} \int_0^\infty dk \, \frac{\tau_{\text{tr}}(\epsilon_\mathbf{k})g(\epsilon_\mathbf{k})}{\epsilon_\mathbf{k}^4}k^4\delta(\epsilon_\mathbf{k} - \epsilon_F) \int_0^\pi d\theta \, 2\pi \sin(\theta)\cos^2(\theta). \tag{5.33}$$

Changing the variable of integration from $\mathbf{k}$ to ϵ and evaluating the integrals gives

$$\sigma_{\text{DC}} = \frac{2}{3}v_F^2 e^2 g(\epsilon_F)\tau_{\text{tr}}(\epsilon_F). \tag{5.34}$$

For a material with donor impurities and no other source of free electrons, the density of impurities is equal to the density of free electrons: $n_i = n$, with $n = N(\epsilon)/V = \frac{\epsilon^3}{6\pi^2\hbar^3 v_F^3}$ from (5.5). The conductivity can then be written as

$$\sigma_{\text{DC}} = \frac{3e^2}{2\pi^3\hbar f(\alpha)}(6\pi^2 n_i)^{1/3}. \tag{5.35}$$

In particular, $\sigma_{\text{DC}} \sim n_i^{1/3}$, another unusual scaling property of the conductivity that is potentially useful as an experimental sign of the Weyl semimetal phase.

5.3 Electron-Electron Interactions

At a low enough concentration of impurities, the results of Section 5.2 break down, as electron-electron interactions become more important than impurity scattering. In this
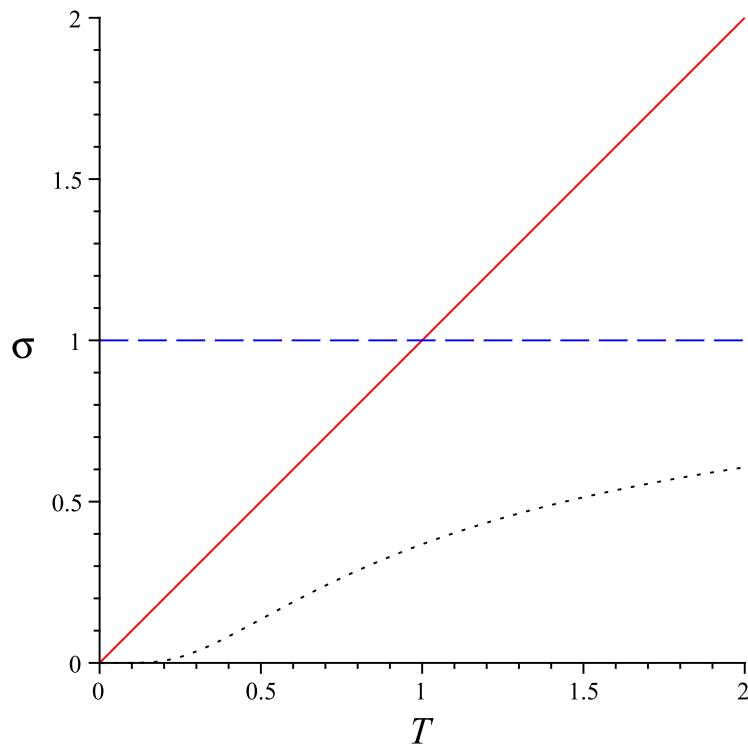
Figure 5.2: Plot of typical low-temperature conductivities for a metal (dashed line) and an insulator (dotted line), compared to that of the Weyl semimetal (solid line), showing that each has behaviour that is qualitatively different from the others. Units are arbitrary.

case, the DC conductivity at low temperatures is given in [3] as

$$\sigma(\omega = n_i = 0) \sim \frac{e^2 T}{h \alpha^2 v_F}. \tag{5.36}$$

This linear dependence of the conductivity on temperature is in sharp contrast to the behaviour of metals, whose conductivities typically approach a constant value for $T \to 0$, and of insulators, which have conductivities decaying as $e^{-T_0/T}$ for some T_0 due to the gap in the electron energy spectrum, as shown in Figure 5.2

5.4   Line Node Semimetal

The line node semimetal also has interesting transport properties, but the calculation of the conductivity is more involved because the density of states is linear in energy, [3] meaning that the Boltzmann equation approach used previously is not valid, as it requires that $1/\tau(\epsilon) \sim g(\epsilon) \ll \epsilon$. The linear density of states means that many of the transport properties of the line node semimetal are similar to those of graphene, which also has a linear density of states. The result from [3] for the conductivity in the presence of point impurities of the form studied in Section 5.1, in the limit $\Delta_S + \Delta_D \gg b \gg |\Delta_S - \Delta_D|$, is

$$\sigma_{xx} = \sigma_{yy} = \frac{e^2 b}{\pi \tilde{v}_F h}, \ \ \sigma_{zz} = \frac{e^2 \tilde{v}_F b}{\pi v_F^2 h}, \tag{5.37}$$

where $\tilde{v}_F = \frac{d}{\hbar}\sqrt{\Delta_S \Delta_D}$ as in Section 4.3.2. The DC conductivity is thus independent of disorder, depending only on the properties of the nodal line. For donor impurities as in Section 5.2, the conductivity is instead

$$\sigma \sim \frac{e^2 v_F^2 n_i}{h \alpha^2 b^2}. \tag{5.38}$$

Chapter 6

Conclusions

This thesis has described in detail two topological materials that are related to and descended from three-dimensional time-reversal invariant topological insulators. These new materials, however, are different in that time-reversal symmetry is violated, and the topological stability is not due to an energy gap but instead due to the separation of Weyl fermions with opposite chiralities in the Weyl semimetal, and discrete symmetries in the line node semimetal. Like topological insulators, the semimetallic phases also have gapless surface states, occurring on a line in momentum space for the Weyl semimetal and in a two-dimensional region of momentum space for the line node semimetal.

The Weyl semimetal has a Hall conductivity $\frac{e^2 k_0}{\pi h}$ that is nearly quantized in the sense that it depends only on the separation $2k_0$ of the Weyl nodes in momentum space. Independent measurements of k_0 and of the Hall conductivity would therefore yield a value for the physical constant e^2/h. The diagonal conductivity due to scattering by Coulomb impurities at zero temperature is proportional to $n_i^{1/3}$, where n_i is the density of impurities. The line node semimetal has a conductivity independent of disorder for point impurities and proportional to n_i for donor impurities.

References

[1] B. Andrei Bernevig, Taylor L. Hughes, and Shou-Cheng Zhang. Quantum spin Hall effect and topological phase transition in HgTe quantum wells. *Science*, 314:1757–1761, December 2006.

[2] A. A. Burkov and Leon Balents. Weyl semimetal in a topological insulator multilayer. *Phys. Rev. Lett.*, 107:127205, Sep 2011.

[3] A. A. Burkov, M. D. Hook, and Leon Balents. Topological nodal semimetals. *Phys. Rev. B*, 84:235126, Dec 2011.

[4] A. H. Castro Neto, F. Guinea, N. M. R. Peres, K. S. Novoselov, and A. K. Geim. The electronic properties of graphene. *Rev. Mod. Phys.*, 81:109–162, Jan 2009.

[5] S. Das Sarma, Shaffique Adam, E. H. Hwang, and Enrico Rossi. Electronic transport in two-dimensional graphene. *Rev. Mod. Phys.*, 83:407–470, May 2011.

[6] P. A. M. Dirac. The quantum theory of the electron. *Proceedings of the Royal Society of London. Series A, Containing Papers of a Mathematical and Physical Character*, 117(778):pp. 610–624, 1928.

[7] A. K. Geim and K. S. Novoselov. The rise of graphene. *Nature Materials*, 6:183–191, March 2007.

[8] V. P. Gusynin and S. G. Sharapov. Transport of dirac quasiparticles in graphene: Hall and optical conductivities. *Phys. Rev. B*, 73:245411, Jun 2006.

[9] F. D. M. Haldane. Model for a quantum Hall effect without Landau levels: Condensed-matter realization of the "parity anomaly". *Phys. Rev. Lett.*, 61:2015–2018, Oct 1988.

[10] M. Z. Hasan and C. L. Kane. *Colloquium*: Topological insulators. *Rev. Mod. Phys.*, 82:3045–3067, Nov 2010.

[11] T. Heikkilä, N. Kopnin, and G. Volovik. Flat bands in topological media. *JETP Letters*, 94:233–239, 2011. 10.1134/S0021364011150045.

[12] C. L. Kane and E. J. Mele. Quantum spin Hall effect in graphene. *Phys. Rev. Lett.*, 95:226801, Nov 2005.

[13] C. L. Kane and E. J. Mele. Z_2 topological order and the quantum spin hall effect. *Phys. Rev. Lett.*, 95:146802, Sep 2005.

[14] Markus König, Steffen Wiedmann, Christoph Brüne, Andreas Roth, Hartmut Buhmann, Laurens W. Molenkamp, Xiao-Liang Qi, and Shou-Cheng Zhang. Quantum spin Hall insulator state in HgTe quantum wells. *Science*, 318:766–770, Nov 2007.

[15] N. B. Kopnin, T. T. Heikkilä, and G. E. Volovik. High-temperature surface superconductivity in topological flat-band systems. arXiv:1103.2033, 2011.

[16] Andreas W. W. Ludwig, Matthew P. A. Fisher, R. Shankar, and G. Grinstein. Integer quantum Hall transition: An alternative approach and exact results. *Phys. Rev. B*, 50:7526–7552, Sep 1994.

[17] Shuichi Murakami. Phase transition between the quantum spin Hall and insulator phases in 3d: emergence of a topological gapless phase. *New J. Phys.*, 9:356, Sept 2007.

[18] K. S. Novoselov, A. K. Geim, S. V. Morozov, D. Jiang, M. I. Katsnelson, I. V. Grigorieva, S. V. Dubonos, and A. A. Firsov. Two-dimensional gas of massless dirac fermions in graphene. *Nature*, 438:197–200, November 2005.

[19] Palash B. Pal. Dirac, majorana, and weyl fermions. *American Journal of Physics*, 79(5):485–498, 2011.

[20] N. M. R. Peres, F. Guinea, and A. H. Castro Neto. Electronic properties of disordered two-dimensional carbon. *Phys. Rev. B*, 73:125411, Mar 2006.

[21] Xiao-Liang Qi and Shou-Cheng Zhang. Topological insulators and superconductors. *Rev. Mod. Phys.*, 83:1057–1110, Oct 2011.

[22] Gordon W. Semenoff. Condensed-matter simulation of a three-dimensional anomaly. *Phys. Rev. Lett.*, 53:2449–2452, Dec 1984.

[23] Nguyen Hong Shon and Tsuneya Ando. Quantum transport in two-dimensional graphite system. *Journal of the Physical Society of Japan*, 67(7):2421–2429, 1998.

[24] Xiangang Wan, Ari M. Turner, Ashvin Vishwanath, and Sergey Y. Savrasov. Topological semimetal and fermi-arc surface states in the electronic structure of pyrochlore iridates. *Phys. Rev. B*, 83:205101, May 2011.

[25] Y. Xia, D. Qian, D. Hsieh, L. Wray, A. Pal, H. Lin, A. Bansil, D. Grauer, Y. S. Hor, R. J. Cava, and M. Z. Hasan. Observation of a large-gap topological-insulator class with a single dirac cone on the surface. *Nature Physics*, 5:398–402, June 2009.

[26] Kai-Yu Yang, Yuan-Ming Lu, and Ying Ran. Quantum hall effects in a weyl semimetal: Possible application in pyrochlore iridates. *Phys. Rev. B*, 84:075129, Aug 2011.

[27] A. A. Zyuzin, M. D. Hook, and A. A. Burkov. Parallel magnetic field driven quantum phase transition in a thin topological insulator film. *Phys. Rev. B*, 83:245428, June 2011.